nature communications

Article

https://doi.org/10.1038/s41467-025-63801-8

Diabetes reshapes pancreatic cancer-associated endothelial niche by accelerating senescence

Received: 29 October 2024

Accepted: 28 August 2025

Published online: 30 September 2025

Check for updates

Yu-Wei Ling[1,2], Juan-Li Duan[1,2], Zi-Jian Jiang[1,2], Zhen Yang[1,2], Jing-Jing Liu[1], Ping Song[1], Zhi-Qiang Fang[1], Zhen-Sheng Yue[1], Fei He[1], Ke-Feng Dou[1] ✉ & Lin Wang[1] ✉

Approximately half of pancreatic cancer patients present with comorbid diabetes. Diabetes is correlated with adverse prognostic outcomes in pancreatic cancer patients, but the underlying mechanism remains elusive. Here, we demonstrate that the cancer-associated endothelial niche is reshaped in the diabetic pancreatic tumor microenvironment and enhances the tumor-promoting capacity. Senescent endothelial cells expand in the diabetic tumor microenvironment and produce a potential senescence-associated secretory phenotype factor, i.e., INHBB. As a member of the TGF-β superfamily, INHBB promotes tumor progression and is regulated by Notch signaling. Pharmacological inhibition of INHBB receptors with bimagrumab effectively inhibited tumor progression in diabetic mice. Moreover, short-term bimagrumab treatment did not significantly decrease glucose levels in diabetic tumor-bearing mice. Combination treatment with metformin showed synergistic antitumor effects. In conclusion, our study identifies INHBB as a promising therapeutic target for pancreatic cancer with comorbid diabetes, laying the foundation for the development of individualized therapies for pancreatic cancer patients.

Pancreatic cancer is considered one of the most lethal malignancies because of its asymptomatic presentation during early stages and inherently aggressive tumor biology. The 5-year survival rate remains poor, predominantly because most patients have advanced, unresectable disease at initial diagnosis[1]. Pancreatic cancer is frequently associated with metabolic comorbidities, including diabetes mellitus, hyperlipidemia and obesity. Current epidemiological data indicate that 35–50% of pancreatic cancer patients exhibit concomitant diabetes[2], and secondary diabetes may develop during disease progression. Notably, diabetes is also correlated with a poor prognosis in these patients[3–5]. These clinical interconnections necessitate further investigation into the characteristics of the diabetes-associated pancreatic tumor microenvironment and the mechanisms through which metabolic dysregulation promotes tumor progression. These insights may facilitate the development of individualized therapeutic strategies for pancreatic cancer patients with diabetes.

Angiogenesis is critical for tumor progression and is a hallmark of cancer[6]. Tumor endothelial cells (TECs) are among the major components of the malignant niche. Beyond mediating blood vessel formation to support tumor growth, TECs facilitate tumor progression, metastasis, and extracellular matrix (ECM) remodeling through the production of cytokines and growth factors such as IL-1β, IL-6, IL-8, FGF4, TGF-β, and Notch signaling ligands[7,8]. TECs also contribute to cancer-associated fibroblast (CAF) formation, immune cell activation and infiltration. TECs exhibit functional heterogeneity in response to environmental stimuli[9,10], particularly under antitumor therapy or metabolic stress conditions[11]. To date, the cell fate and phenotypic

[1]Department of Hepatobiliary Surgery, Xijing Hospital, Fourth Military Medical University, Xi'an, China. [2]These authors contributed equally: Yu-Wei Ling, Juan-Li Duan, Zi-Jian Jiang, Zhen Yang. ✉e-mail: doukef@fmmu.edu.cn; fierywang@163.com

plasticity of TECs within the tumor microenvironment remain to be fully elucidated.

Cellular senescence is a permanent state of cell cycle arrest[12] and was historically considered to act as a barrier to tumorigenesis. Oncogene-induced senescence (OIS), a well-established mechanism in the tumor microenvironment, occurs when oncogenic drivers (such as $Hras^{G12V}$, $Kras^{G12V}$, $Nras^{Q61R}$ in the RAS/MAPK pathway, or $PIK3CA^{H1047R}$, $AKT1^{E17K}$ mutations and PTEN loss in the PI3K/AKT pathway) are ectopically expressed, inducing senescence in stromal or neoplastic cells[13]. Recent studies have indicated that Notch signaling regulates OIS. Ectopic expression of the Notch intracellular domain (NICD) activates Notch signaling, triggering cell-autonomous senescence, termed Notch-induced senescence (NIS)[14]. In addition to senescence arresting transformation in premalignant cells, senescent cells exhibit immunogenicity and can stimulate antitumor immunity[15–17]. Nevertheless, emerging evidence suggests that senescent cells within tumors may accelerate cancer progression[18]. These cells remain metabolically active and secrete cytokines and growth factors, collectively termed the senescence-associated secretory phenotype (SASP)[19]. Senescent cancer-associated fibroblasts (CAFs) and macrophages are widely reported to promote tumor progression, treatment resistance, and immunosuppression through the activity of inflammatory factors such as IL-1β, IL-6, IL-8, IL-10, IL-33, HGF, and CCL2[20–26]. Tumor endothelial cells (TECs) can also undergo senescence in response to chemotherapeutic agents or ionizing radiation[27,28]. Similarly, senescent TECs secrete cytokines that modulate the tumor microenvironment[18]. Diabetes is reported to be associated with endothelial cell senescence[29–33]. However, the properties of diabetic TECs and the functional role of senescent TECs in tumors remain poorly characterized.

In this study, we demonstrate that diabetes reshapes the cancer-associated endothelial niche. Tumor endothelial cells undergo senescence and secrete INHBB as a SASP factor that promotes pancreatic cancer progression. Targeting the INHBB receptor activin receptor type II (ActRII) with bimagrumab, a monoclonal antibody previously evaluated for obesity treatment that acts by regulating skeletal muscle growth and fat consumption, significantly attenuated tumor progression in diabetic mice. Collectively, our findings provide a potential therapeutic rationale for targeted therapies in pancreatic cancer patients with concomitant diabetes.

Results

Diabetes is associated with pancreatic cancer progression and poor prognosis

First, we analyzed pancreatic cancer patient cohorts from the publicly available MSK-IMPACT database and our institution's clinicopathological data (Xijing Hospital cohort). In the MSK-IMPACT cohort, records of 2336 PDAC patients were collected; 2270 had overall survival records, and 1418 had records of whether they have diabetes or not. After 918 metastatic and 114 locally advanced PDAC patients were excluded, 386 patients were included (273 without diabetes and 113 with diabetes). KRAS mutations were present in 94.8% of the tumors (Supplementary Table 1). Following normality testing for continuous variables (Supplementary Fig. 1a), baseline characteristics were compared between groups. The proportion of patients with hypertension and coronary artery disease was greater in the diabetes group, whereas other characteristics were not significantly different (Supplementary Table 1). Multivariate Cox regression analysis revealed diabetes and mutation count as independent predictors of poor overall survival in patients with primary PDAC (Table 1). Kaplan–Meier analysis confirmed that patients with diabetes had worse overall survival than those without diabetes (Fig. 1a).

In the Xijing Hospital cohort, we included 339 PDAC patients who underwent surgery. We excluded 21 patients with locally advanced tumors identified intraoperatively and 35 patients whose follow-up records were missing. Additionally, 12 patients lacking fasting blood glucose records and 3 patients without documentation about diabetes history were excluded, yielding 268 patients for analysis. Following normality testing for continuous variables (Supplementary Fig. 1b), patients in the diabetes group exhibited higher fasting blood glucose levels, elevated CA199 and CEA levels, and a greater proportion of T3-stage tumors (Supplementary Table 2). Multivariate Cox regression revealed that diabetes, higher CA199 levels, larger tumor size, and more metastatic lymph nodes were independent predictors of worse overall survival in PDAC patients (Table 2). Kaplan–Meier analysis confirmed worse overall survival in patients with diabetes than in those without diabetes (Fig. 1b). Furthermore, a preoperative glucose concentration ≥6.1 mmol/L significantly worsened 2-year overall survival but did not significantly affect overall survival across the entire follow-up period (Supplementary Fig. 1c, d). These findings suggest that systemic metabolic and pathological abnormalities in patients with diabetes, rather than hyperglycemia alone, are key contributors to poor PDAC outcomes.

Diabetes promotes pancreatic cancer progression in mouse models

The role of diabetes in pancreatic cancer progression was further verified using mouse models. First, we constructed 4 mouse models representing different stages of diabetes (Fig. 1c). Intraperitoneal glucose tolerance tests (IPGTTs) revealed impaired glucose tolerance in the 16-week high-fat diet (HFD) and HFD+streptozotocin (STZ) groups (Fig. 1d, e). However, 16 weeks of HFD consumption resulted in increased body weight but only mild fasting blood glucose elevation, fluctuating around the diagnostic threshold for murine diabetes, which is consistent with prediabetes and early-stage diabetes (Fig. 1d–g). HFD + STZ mice exhibited significantly elevated blood glucose levels and abnormal glucose tolerance (Fig. 1d–g). Next, orthotopic pancreatic cancer progression was monitored across models. Insulin glargine was administered to HFD + STZ mice to eliminate the effects of STZ on tumors and successfully stabilized blood glucose (Fig. 1h). Accelerated tumor growth occurred in the 16-week HFD and HFD + STZ groups, with tumors displaying irregular, multifocal morphology in the HFD + STZ group. Insulin treatment suppressed tumor growth in HFD + STZ mice (Fig. 1i–k). Similarly, in the Pan02 graft model, compared with chow-fed control mice, tumor-bearing HFD + STZ mice showed a greater tumor burden and higher mortality rate (Supplementary Fig. 1e–h). Collectively, these results demonstrate that diabetes promotes pancreatic tumor progression and worsens prognosis.

Diabetes reshapes the tumor endothelial niche

We conducted bulk RNA-seq analysis on Pan02 tumor tissues from the HFD + STZ and chow groups. PCA revealed distinct intergroup differences (Supplementary Fig. 2a). Differentially expressed genes (DEGs) were identified (Supplementary Fig. 2b, Supplementary Data 1), and pathway enrichment analysis revealed significant alterations in extracellular matrix organization and immune pathways (Supplementary Fig. 2c). We also analyzed bulk RNA-seq data from the GEO database (GSE266899) for KPC tumors in control (low-fat rodent chow, LFD) and diabetic (HFD) mice (Supplementary Fig. 2d, e). Pathway enrichment analysis revealed DEGs associated with extracellular matrix organization (Supplementary Fig. 2f, Supplementary Data 2). The cancer-associated endothelial niche critically influences tumor progression. RNA-seq revealed that tumor endothelial disorganization-related genes[34] were enriched in the diabetic microenvironment (Fig. 2a, b, Supplementary Fig. 2g, h), suggesting that the tumor endothelial niche was disrupted by metabolic dysregulation. Immunofluorescence staining (Fig. 2c, d) and flow cytometry (Fig. 2e, f, Supplementary Fig. 2i) confirmed the increased vascular density in diabetic tumors. To assess the effects of diabetes-exposed TECs on tumor progression, we performed in vivo and in vitro coculture assays (Fig. 2g). Coinjection of TECs and KPC cells into chow-fed C57BL/6J mice did not alter fasting

https://doi.org/10.1038/s41467-025-63801-8

Table 1 | Cox regression for overall survival in primary pancreatic cancer patients from the MSK-IMPACT cohort

Variables		Univariate Cox regression		Multivariate Cox regression	
		Hazard ratio (95% CI)	*P*-value	Hazard ratio (95% CI)	*P*-value
Age (years)		1.005 (0.993–1.018)	0.388		
Sex	Female	1.000	0.443		
	Male	1.107 (0.854–1.435)			
Diabetes	Without	1.000	0.021	1.000	0.041
	With	1.376 (1.049–1.805)		1.328 (1.011–1.743)	
Autoimmune disease	Without	1.000	0.957		
	With	0.985 (0.573–1.693)			
Coronary artery disease	Without	1.000	0.055		
	With	1.424 (0.993–2.042)			
Hypertension	Without	1.000	0.972		
	With	1.005 (0.775–1.302)			
Pancreatitis	Without	1.000	0.960		
	With	1.010 (0.671–1.521)			
Cancer history	False	1.000	0.397		
	True	0.887 (0.672–1.171)			
Smoking	False	1.000	0.266		
	True	1.160 (0.893–1.505)			
Tumor location	Head	1.000	0.855		
	Body/tail	1.027 (0.768–1.373)			
Neoadjuvant therapy	False	1.000	0.092		
	True	1.570 (0.929–2.652)			
Mutation count		1.080 (1.032–1.130)	0.001	1.076 (1.027–1.129)	0.002
Mutation	KRAS	1.000			
	MAPK	0.772 (0.343–1.738)	0.532		
	Wild type	0.701 (0.289–1.703)	0.433		
Tumor purity		1.568 (0.551–4.465)	0.400		

blood glucose levels (Fig. 2h). TECs from tumors in HFD + STZ mice accelerated in vivo tumor progression (Fig. 2i–k) and increased Ki-67 expression compared with TECs from tumors in chow-fed mice (Fig. 2l, m). Conditioned medium (CM) from HFD + STZ TECs moderately increased proliferation but significantly promoted KPC cell migration (Fig. 2n–p). The Pan02 models yielded similar results (Supplementary Fig. 2j–r). These findings prompted further investigation into diabetic TEC heterogeneity.

Diabetic TEC clusters exhibit a senescent phenotype

Diabetes is a major inducible factor for cellular senescence, as hyperglycemia and abnormal lipid deposition promote oxidative stress, which triggers senescence. Although the pancreatic cancer microenvironment is not typically considered lipid-rich[35], we observed abnormal lipid deposition in HFD + STZ tumors (Fig. 3a), suggesting its potential role in senescence induction. We analyzed scRNA-seq data from PDAC patients in the GSA database (CRA001160; 14 patients without diabetes and 10 patients with diabetes). After data integration and doublet removal, major cell types were annotated according to a previously described method[36]. Ductal cell type 2 represented malignant cells (Supplementary Fig. 3a, b). The distribution of cells among individual patients is shown in Supplementary Fig. 3c. Endothelial cells were isolated and clustered into 7 subpopulations under unsupervised clustering (C1–C7; Fig. 3b). Cluster-specific markers are listed in Supplementary Data 3. Violin plots revealed positive CD45 expression in cluster C7 (indicating immune cell contamination), whereas PROX1 (a lymphatic marker) was absent in clusters C1–C6 (Fig. 3c). DEGs between control and diabetic endothelial cells were identified (Supplementary Data 4). Based on established endothelial markers[37], we classified C1–C3 as capillary (C1: 2173; C2: 722; C3: 692 cells), C4–C5 as venous (C4: 461; C5: 376 cells), and C6 as arterial (66 cells) (Fig. 3d). Cluster C3 exhibited the highest endothelial senescence score, with low proliferation/apoptosis scores and elevated fatty acid metabolism/oxidation scores (Fig. 3d). Thus, C1–C6 were defined as distinct endothelial subsets, with C3 identified as senescent capillary cells that expanded in diabetic microenvironments (Fig. 3e). CellChat analysis demonstrated strong interactions between senescent capillary cells and malignant ductal cells in the diabetic pancreatic cancer microenvironment (Supplementary Fig. 3d), with potential ligand–receptor interactions shown in Supplementary Fig. 3e. These findings suggest that senescent endothelial cells regulate cancer cell phenotypes.

We further verified these findings in mouse tumor models. GSEA revealed enrichment of the pancancer endothelial cell senescence signature in Pan02 and KPC tumors from diabetic models (Supplementary Fig. 3f, g). scRNA-seq analysis was performed on mouse tumors, with major cell types identified using specific markers (Fig. 3f, g). TECs composed only a minor fraction of the total cells (265 endothelial cells: 52 cells in the chow group, 213 cells in the HFD + STZ group), which was insufficient for further clustering. Nevertheless, endothelial cells from diabetic tumors exhibited elevated senescence levels (Fig. 3h). TECs in diabetic tumor microenvironments presented increased lipid metabolism-related molecule expression and decreased proliferation marker expression (Fig. 3i). The senescence signature was also enriched in diabetic TECs (Fig. 3j). Cell cycle analysis revealed fewer TECs in the G2M phase in diabetic models (Fig. 3k). Immunofluorescence staining confirmed increased $P16^{+}CD31^{+}$ cells in HFD + STZ tumors (Fig. 3l, m). Flow cytometry demonstrated a twofold increase in senescent endothelial cells ($CD45^{-}CD31^{+}SA\text{-}\beta\text{-}Gal^{+}$) in

https://doi.org/10.1038/s41467-025-63801-8

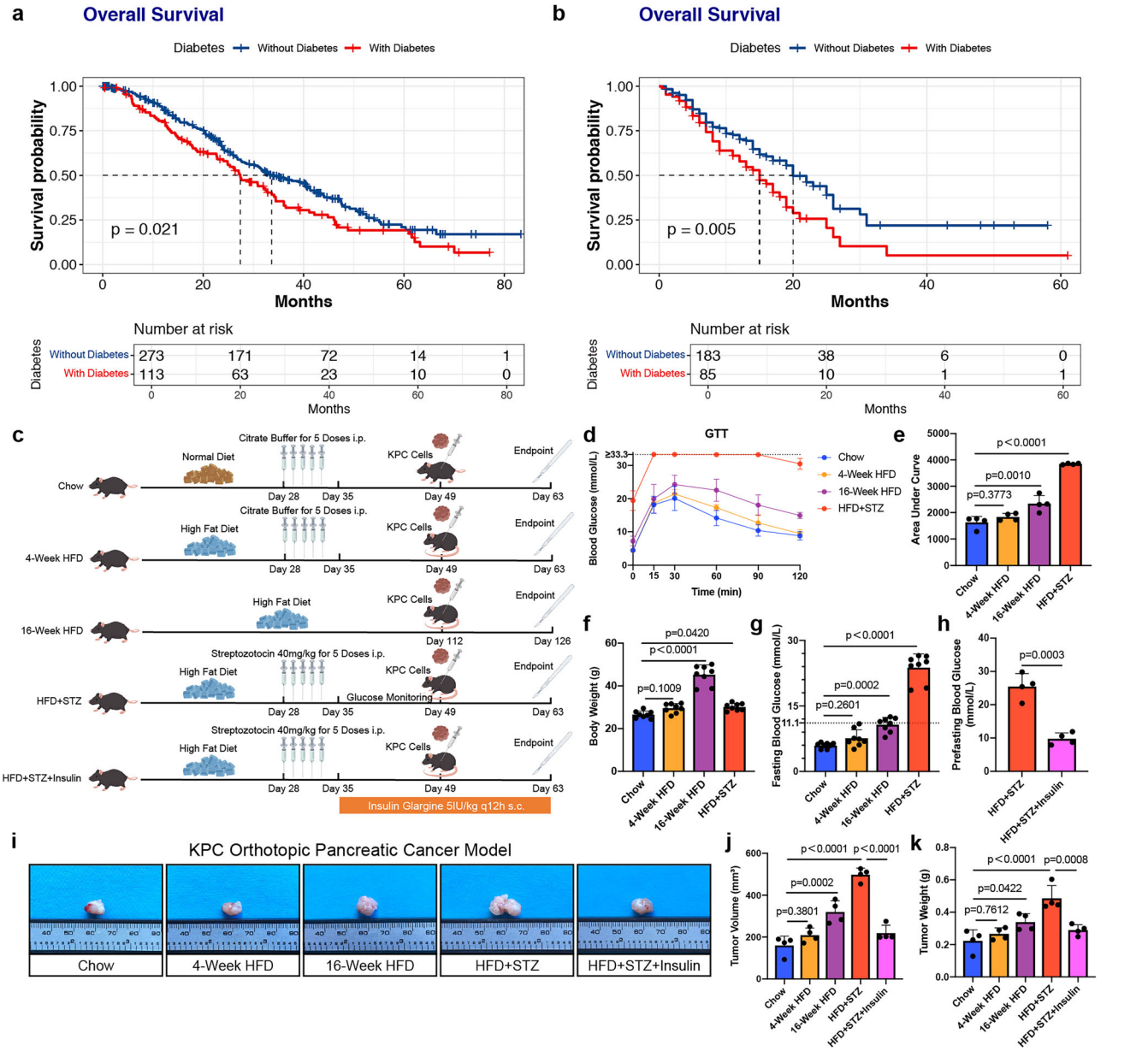

Fig. 1 | Diabetes accelerates pancreatic cancer progression and is associated with a poor prognosis. a Kaplan–Meier survival curves depicting the overall survival of patients with primary resectable pancreatic ductal adenocarcinoma in the MSK-IMPACT cohort ($n = 386$ patients; $n = 273$ without diabetes, $n = 113$ with diabetes). **b** Kaplan–Meier survival curves depicting the overall survival of patients with primary resectable pancreatic ductal adenocarcinoma in the Xijing Hospital cohort ($n = 268$ patients; $n = 183$ without diabetes, $n = 85$ with diabetes). **c** Schematic representation of tumor-bearing models in C57BL/6J mice (by figdraw.com). **d** Blood glucose change curves during the IPGTT ($n = 4$ mice per group). **e** Bar graphs showing the area under the curve for the IPGTT ($n = 4$ mice per group). **f** Bar graphs showing body weights in different mouse models ($n = 8$ mice per group). **g** Bar graphs showing fasting blood glucose levels in different mouse models ($n = 8$ mice per group). **h** Bar graphs comparing prefasting blood glucose levels between HFD + STZ mice and insulin-treated mice ($n = 4$ mice per group). **i** Representative images of orthotopic pancreatic tumors in the normal diet (chow), 4-week HFD, 16-week HFD, HFD + STZ and HFD + STZ + Insulin groups ($n = 4$ mice per group). **j** Bar graphs showing tumor volumes in different mouse models ($n = 4$ mice per group). **k** Bar graphs showing tumor weights in different mouse models ($n = 4$ mice per group). IPGTT intraperitoneal glucose tolerance test. The bars represent the means ± SDs. *P*-values were determined by the log-rank test (**a**, **b**), one-way ANOVA (**e**–**g**, **j**, **k**) and two-tailed unpaired *t*-test (**h**). Source data are provided as a Source Data file.

HFD + STZ tumors (Fig. 3n, o, Supplementary Fig. 2i). Finally, the senescence markers Trp53 (p53), Cdkn1a (p21), and Cdkn2a (p16) were upregulated in primary TECs isolated from HFD + STZ tumors (Fig. 3p, Supplementary Fig. 3 h). These results demonstrate that diabetes promotes TEC senescence in tumor microenvironments.

Senescent endothelial cells facilitate tumor progression

To determine whether senescent endothelial cells promote tumor progression, we first induced senescence in HUVECs using hydrogen peroxide (HO, 300 μM) and high glucose (HG, 25 mmol/L) + palmitic acid (PA, 300 μmol/L). Senescence was confirmed by SA-β-Gal staining and elevated senescence/SASP marker expression (Supplementary Fig. 4a–f). Consistently, coculture with senescent HUVECs moderately increased proliferation but significantly increased PANC-1 cell migration (Fig. 4a–f). These results indicate that senescent endothelial cells promote tumor progression via angiocrine mechanisms. We next eliminated senescent cells using ABT-263 (100 mg/kg, oral gavage, once daily for 7 days) in diabetic tumor-bearing mice (Fig. 4g,

Table 2 | Cox regression for overall survival in primary pancreatic cancer patients from the Xijing Hospital cohort

Variables		Univariate Cox regression		Multivariate Cox regression	
		Hazard ratio (95% CI)	*P*-value	Hazard ratio (95% CI)	*P*-value
Age (years)		1.009 (0.989–1.030)	0.363		
BMI		0.946 (0.888–1.007)	0.083		
Sex	Female	1.000	0.288		
	Male	0.823 (0.575–1.179)			
Diabetes	Without	1.000	0.006	1.000	0.035
	With	1.649 (1.156–2.354)		1.496 (1.030–2.173)	
Pancreatitis	Without	1.000	0.488		
	With	1.311 (0.609–2.820)			
Smoking	False	1.000	0.120		
	True	1.346 (0.926–1.957)			
ALT (U/L)		1.0007 (0.9994–1.0020)	0.261		
GGT (U/L)		1.0001 (0.9997–1.0004)	0.782		
CA199 (U/mL)		1.0001 (1.0000–1.0001)	0.005	1.0001 (1.0000–1.0001)	0.009
CEA (ng/mL)		1.0012 (1.0003–1.0021)	0.012	1.0007 (0.9997–1.0017)	0.149
Vessel invasion	False	1.000	0.485		
	True	1.169 (0.754–1.813)			
Nerve infiltration	False	1.000	0.317		
	True	1.205 (0.836–1.735)			
Fat tissue invasion	False	1.000	0.805		
	True	1.054 (0.695–1.599)			
Tumor maximum diameter (cm)		1.124 (1.010–1.252)	0.033	1.133 (1.012–1.268)	0.031
T stage	T1	1.000			
	T2	1.289 (0.773–2.152)	0.331		
	T3	1.701 (0.937–3.090)	0.081		
Number of metastatic lymph nodes		1.091 (1.020–1.167)	0.011	1.096 (1.024–1.172)	0.008

Supplementary Fig. 4g). ABT-263 significantly reduced the tumor burden without affecting blood glucose levels in the KPC and Pan02 models (Fig. 4h–k, Supplementary Fig. 4h–k). Additionally, SA-β-Gal$^+$ cells were effectively eliminated after ABT-263 treatment (Supplementary Fig. 4l, m). P16$^+$CD31$^+$ cells were increased in HFD + STZ KPC tumors and decreased by 61.3% after ABT263 treatment (Fig. 4l, m). Senescent endothelial cells were also decreased in Pan02 graft models (Supplementary Fig. 4n, o). However, specific senescent endothelial cell targeting remains challenging. Senolytics systemically deplete senescent cells, potentially eliminating beneficial populations involved in wound healing, vascularization, tissue regeneration, and insulin secretion[38–40], and may cause thrombocytopenia and neutropenia[41]. We therefore sought to identify specific SASP factors secreted by senescent TECs.

Notch signaling is activated in senescent TEC clusters

Notch signaling is a critical pathway that regulates endothelial cell fate. Our previous work demonstrated that Notch signaling regulates senescence in liver sinusoidal endothelial cells[42]. scRNA-seq data revealed the enrichment of multiple Notch signaling pathways in senescent capillary endothelial clusters (Fig. 5a). The expression of the Notch target genes HES1 and HEY1 was upregulated in TECs from diabetic microenvironments and different senescent endothelial models (Fig. 5b–e, Supplementary Fig. 3h). Reportedly, ectopic NICD overexpression activates Notch signaling and induces HUVEC senescence[43]. Analysis of RNA-seq data from endothelial-specific NICD-overexpressing TECs (GEO: GSE111127) revealed the upregulated expression of senescence markers and decreased expression of Mki67 in Notch-activated TECs (Fig. 5f). We inhibited Notch signaling in proliferating and senescent HUVECs using the γ-secretase inhibitor DAPT (10 μM). qPCR confirmed that DAPT effectively blocked Notch signaling in both states. Notch inhibition reduced p21 expression but did not affect p16 expression (Fig. 5g). SA-β-Gal staining revealed decreased proportions of senescent cells (Fig. 5h, Supplementary Fig. 5a), indicating partial suppression of endothelial senescence by Notch inhibition. Critically, DAPT treatment significantly attenuated the protumoral paracrine effects of senescent HUVECs on tumor migration and proliferation (Fig. 5i, j, Supplementary Fig. 5b). Thus, Notch activation promotes endothelial senescence and specifically facilitates protumoral SASP production.

INHBB is a SASP factor secreted by senescent endothelial cells

To identify effector molecules produced by senescent TECs, we performed an intersection analysis between senescent capillary endothelial cluster markers (115 genes), upregulated genes in diabetic TECs (2397 genes), upregulated genes in diabetic tumors (849 genes) and a secretory factor gene set (343 genes). INHBB was upregulated across all the gene sets (Fig. 6a). INHBB (inhibin subunit βB), a member of the TGF-β superfamily, exhibited endothelial-specific expression (Fig. 6b). INHBB expression was positively correlated with endothelial senescence scores in human and mouse TECs (Fig. 6c) and was upregulated in TECs from diabetic microenvironments and different senescent HUVEC models (Fig. 6d, e, Supplementary Fig. 3h). Inhbb and its homodimer Activin B were elevated in diabetic tumors (Fig. 6f–h). INHBB$^+$ endothelial cell populations were expanded in HFD + STZ KPC tumors and were reduced by ABT-263 treatment (Fig. 6i, j). The Pan02 models showed similar changes (Supplementary Fig. 5c–f). These results indicate that INHBB is a potential SASP factor secreted by senescent endothelial cells.

We sought to clarify whether INHBB contributes to tumor progression. Analysis of data from the GEPIA2 database revealed higher INHBB expression in PDAC tissues than in normal pancreatic tissues

https://doi.org/10.1038/s41467-025-63801-8

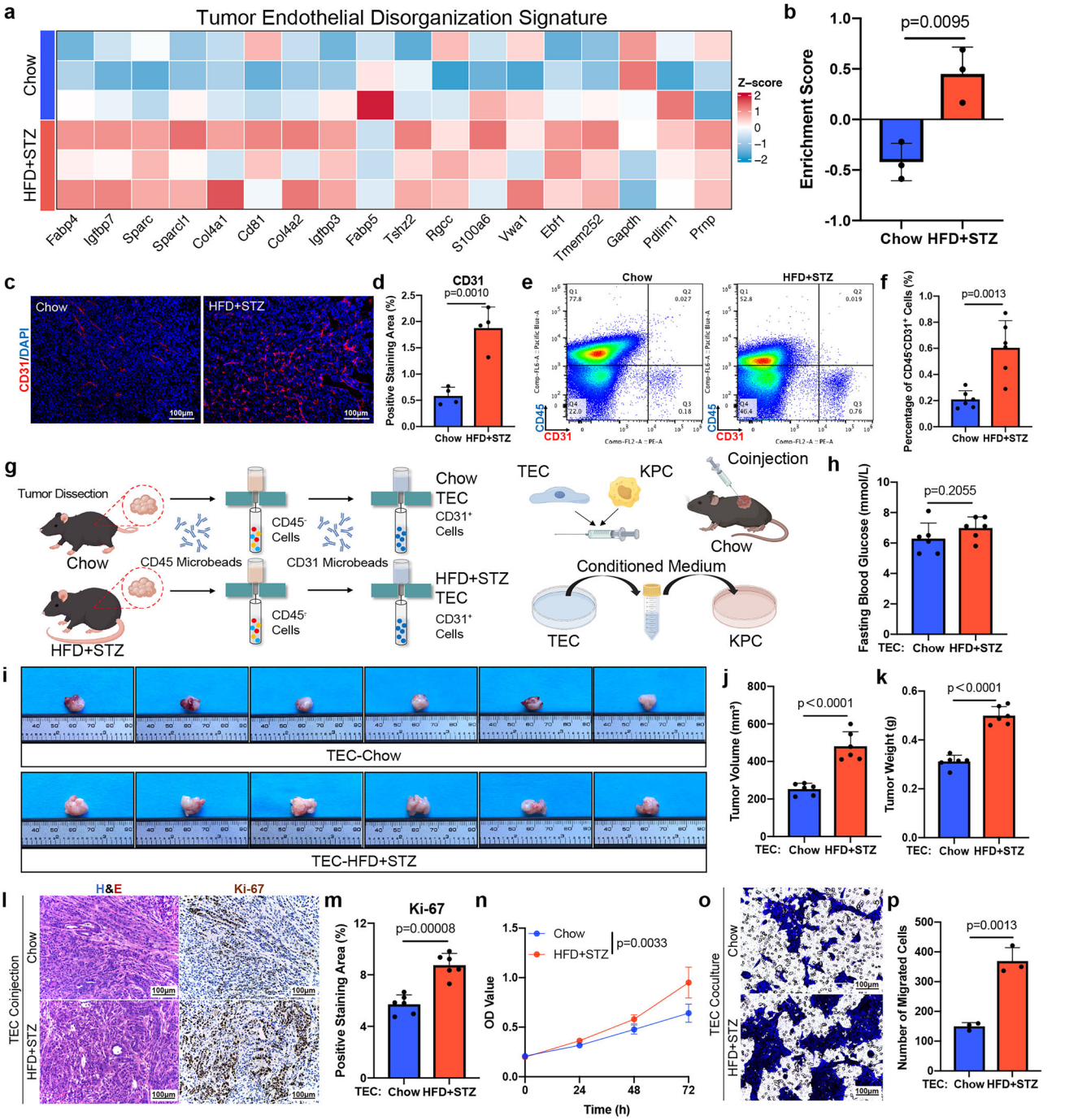

Fig. 2 | Tumor endothelial cells in the diabetic tumor microenvironment promote the progression of pancreatic cancer. a Heatmap showing the expression of tumor endothelial disorganization signature genes in tumor samples collected from chow and HFD + STZ mice based on bulk RNA-seq data ($n = 3$ mice per group). **b** Bar graph showing the GSVA scores for the tumor endothelial disorganization signature in chow and HFD + STZ tumors ($n = 3$ mice per group). **c**, **d** Representative images (**c**) and quantification (**d**) of immunofluorescence staining for CD31 (red) in chow and HFD + STZ tumor tissues ($n = 4$ mice per group). **e** Proportion of $CD45^-CD31^+$ cells in tumors quantified using flow cytometry. **f** Bar graph showing the percentage of $CD45^-CD31^+$ tumor endothelial cells in chow and HFD + STZ tumor tissues ($n = 6$ mice per group). **g** Schematic representation of primary tumor endothelial cell isolation and in vitro/in vivo coculture experiments (by figdraw.com). **h** Bar graph showing fasting blood glucose levels in chow-TEC/HFD + STZ-TEC and KPC coinjected tumor tissues ($n = 6$ mice per group). **i** Orthotopic pancreatic tumor samples from chow-TEC/HFD + STZ-TEC and KPC coinjected tumor tissues ($n = 6$ mice per group). **j** Bar graph showing tumor volumes in the chow-TEC/HFD + STZ-TEC and KPC coinjected groups ($n = 6$ mice per group). **k** Bar graph showing tumor weights in the chow-TEC/HFD + STZ-TEC and KPC coinjected groups ($n = 6$ mice per group). **l**, **m** Representative images (**l**) and quantification (**m**) of H&E and immunohistochemical staining for Ki-67 (brown) in chow-TEC/HFD + STZ-TEC and KPC coinjected tumor tissues ($n = 6$ mice per group). **n** Line graph showing OD values from CCK-8 proliferation assays for KPC cells cocultured with TECs isolated from chow or HFD + STZ tumor-bearing mice ($n = 3$ biologically independent samples per group). **o**, **p** Representative images (**o**) and quantification (**p**) of migrated KPC cells cocultured with TECs isolated from chow or HFD + STZ tumor-bearing mice in Transwell migration assays ($n = 3$ biologically independent samples per group). OD optical density, H&E hematoxylin & eosin, TEC tumor endothelial cell. The bars represent the means ± SDs. *P*-values were determined by the two-tailed unpaired *t*-test (**b**, **d**, **f**, **h**, **j**, **k**, **m**, **p**) and two-way ANOVA (**n**). Source data are provided as a Source Data file.

https://doi.org/10.1038/s41467-025-63801-8

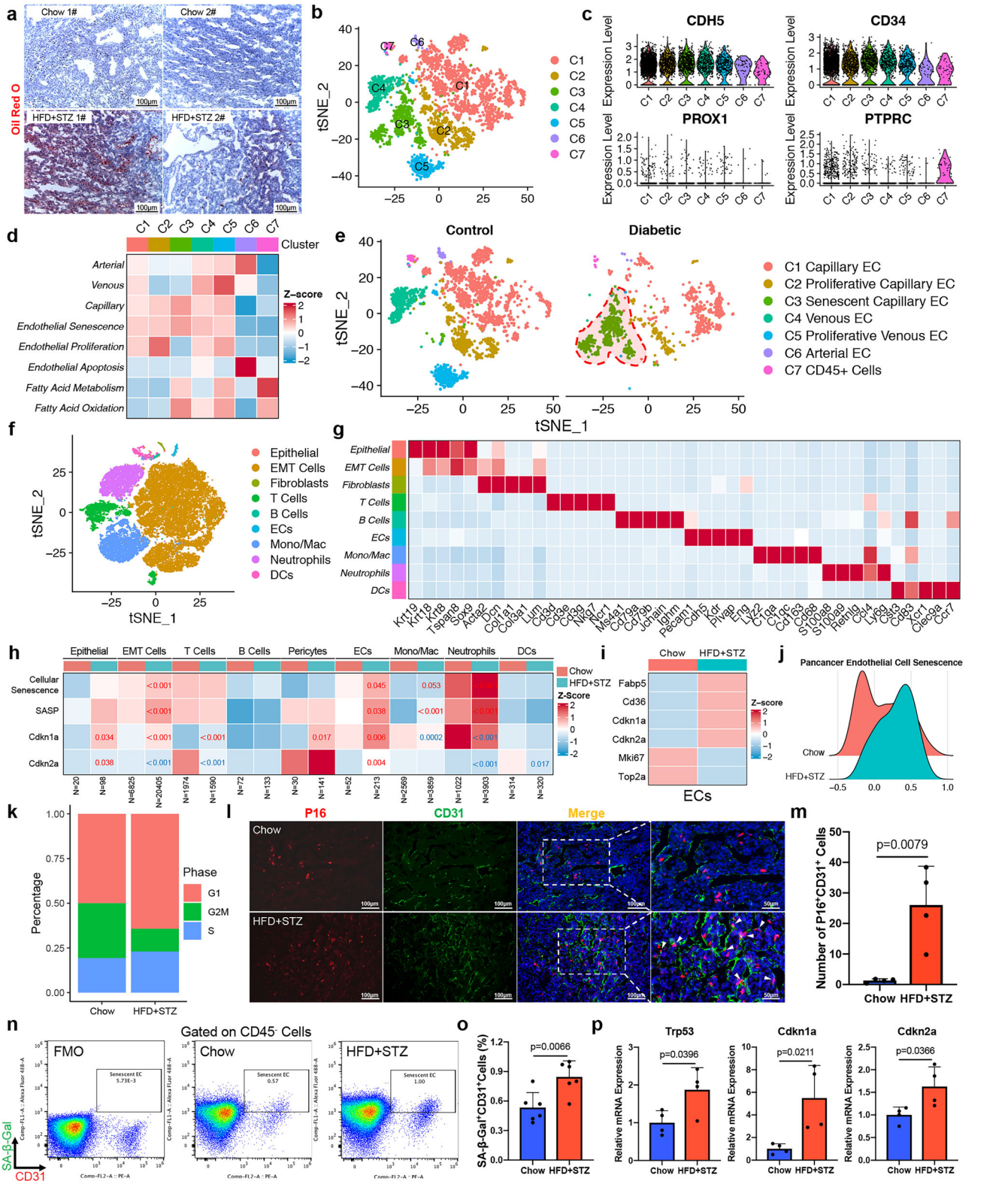

(Fig. 6k). High tumoral INHBB expression correlated with poor overall survival and disease-free survival in PDAC patients (Kaplan–Meier plotter database; Fig. 6l). The activin pathway was enriched in diabetic tumor microenvironments (Fig. 6m). These findings suggest that INHBB may regulate the tumor microenvironment. Recombinant Activin B moderately increased proliferation but significantly increased the migratory capacity of pancreatic cancer cells (Fig. 6n–p). Phosphorylated Smad2 levels increased after Activin B stimulation (Fig. 6q). Collectively, our results indicate that endothelium-derived INHBB promotes pancreatic cancer progression.

Notch signaling regulates INHBB expression

Since Notch signaling was enriched in the senescent endothelial cell cluster, we investigated whether Notch signaling modulates the expression of INHBB. We found that the expression of INHBB was positively correlated with the Notch signaling score based on scRNA-

Fig. 3 | Diabetes reshapes the cancer-associated endothelial niche by accelerating senescence. a Representative images of oil red O staining (red) of pancreatic tumor tissues from chow-fed and HFD + STZ mice. **b** t-SNE plot showing unsupervised clustering of endothelial cells based on scRNA-seq data in the GSA database (CRA001160). **c** Violin plots showing the expression of CDH5, CD34, PROX1, and PTPRC in different endothelial cell clusters. **d** Heatmap showing scores for arterial, venous, capillary, endothelial senescence, proliferation, apoptosis, fatty acid metabolism and oxidation terms in different endothelial cell clusters. **e** t-SNE plot showing endothelial clusters in PDAC patient samples. **f** t-SNE plot showing major cell types in pancreatic tumors from chow and HFD + STZ mice. **g** Heatmap showing specific markers of major cell types. **h** Heatmap showing Cdkn1a, Cdkn2a expression and senescence scores for major cell types. *P*-values in blue indicate downregulation, those in red indicate upregulation, and '*N*' indicates cell numbers. **i** Heatmap showing the expression of Fabp5, Cd36, Cdkn1a, Cdkn2a, Mki67, and Top2a in TECs from chow and HFD + STZ mice. **j** Ridge plot showing the endothelial senescence scores of TECs from chow and HFD + STZ mice. **k** Cell cycle analysis of TECs from chow and HFD + STZ tumors. **l**, **m** Representative images (**l**) and quantification (**m**) of immunofluorescence staining for P16 (red) and CD31 (green) in chow and HFD + STZ tumors. **n**, **o** Representative images (**n**) and quantification (**o**) of proportion of $CD45^-CD31^+SA\text{-}\beta\text{-}Gal^+$ cells in tumors quantified by flow cytometry ($n = 6$ mice per group). **p** Bar graphs showing the mRNA expression of Trp53, Cdkn1a, and Cdkn2a in TECs isolated from KPC tumors from chow and HFD + STZ mice. t-SNE t-distributed stochastic neighbor embedding, TEC tumor endothelial cell, EC endothelial cell, EMT epithelial–mesenchymal transition, Mono/Mac monocytes/macrophages. The bars represent the means ± SDs. **b**–**e** $n = 14$ patients in the control group and $n = 10$ patients in the diabetic group. **f**–**k** $n = 2$ mice in the chow group and $n = 4$ mice in the HFD + STZ group. **a**, **l**, **m**, **p**, $n = 4$ mice per group. *P*-values were determined by the Mann–Whitney test (**h**) and two-tailed unpaired *t*-test (**m**, **o**, **p**). Source data are provided as a Source Data file.

seq data (Fig. 7a). INHBB was identified as one of the top upregulated genes in DLL4 (a Notch ligand)-stimulated endothelial cells[44]. Published data also revealed that INHBB expression was upregulated in NICD (Notch intracellular domain) knock-in TECs (GSE111127), DLL4-stimulated HUVECs (GSE163568), and Jagged-1 (a Notch ligand)-overexpressing HUVECs (GSE40403) (Fig. 7b). We also found that incubation with DLL4-Fc to activate Notch signaling in HUVECs upregulated INHBB expression (Fig. 7c). Consistent with these findings, we observed that INHBB expression was downregulated in senescent HUVECs following the blockade of Notch signaling (Fig. 7d–f).

We then generated $RBPJ^{ECKO}$ genetically modified mice to specifically disrupt RBPJ-mediated Notch signaling in endothelial cells. As shown in Fig. 7g–i, disruption of Notch/RBPJ in endothelial cells inhibited pancreatic tumor growth. Moreover, in a rescue experiment, Pan02 cells coinjected with recombinant Activin B into $RBPJ^{ECKO}$ mice restored tumor growth. Furthermore, endothelial Notch deficiency resulted in a decrease in the number of senescent cells (Fig. 7j, k) and INHBB expression (Fig. 7l, m) in the tumor microenvironment. These data collectively indicate that endothelial Notch signaling regulates INHBB expression and pancreatic cancer progression.

Bimagrumab inhibits diabetic pancreatic cancer progression

Because targeting endothelial Notch signaling or specifically eliminating senescent TECs is difficult to achieve for translational therapy in vivo, we aimed to discover agents targeting the SASP factor INHBB. According to the results of the CellChat analysis, the INHBB-ActRII pathway mediated the interaction between senescent TECs and cancer cells (Supplementary Fig. 3e). Bimagrumab, which blocks both the INHBB receptors ActRIIA and ActRIIB, was tested in a phase II randomized clinical trial in adults with type 2 diabetes and obesity for improving body composition and insulin sensitivity[45]. However, there is no evidence supporting bimagrumab for the effective treatment of solid tumors except against cachexia. We observed the antitumor effect of bimagrumab in KPC and Pan02 pancreatic cancer models (Fig. 8a, Supplementary Fig. 6a). Similarly, we found that bimagrumab increased the body weight of tumor-bearing mice, which is consistent with its reported effect against cachexia (Fig. 8b, Supplementary Fig. 6b). No antitumor effects were observed in tumor-bearing mice fed a normal diet (Fig. 8c–e, Supplementary Fig. 6c, d). Surprisingly, two doses of bimagrumab (20 mg/kg, subcutaneous injection, once weekly) diminished the tumor burden in diabetic mice (Fig. 8c–e, Supplementary Fig. 6c, d) without significantly reducing blood glucose levels (Fig. 8f, Supplementary Fig. 6e). These findings suggest that the therapeutic effect of bimagrumab does not depend on improving hyperglycemia. We also found that the weight of the bilateral tibialis anterior muscles increased after bimagrumab administration (Fig. 8g, h). As INHBB leads to the upregulation of phosphorylated Smad2 in cancer cells, we found that phosphorylated Smad2 was upregulated in diabetic tumors and that bimagrumab treatment inhibited Smad2 phosphorylation in diabetic mice (Supplementary Fig. 6f–i). Because Smad activation is associated with tumor fibrosis, picrosirius red and α-SMA staining both indicated that tumor fibrosis in diabetic mice was significantly alleviated after bimagrumab administration (Fig. 8i–l). Furthermore, combination treatment with metformin inhibited the progression of hyperglycemia during the tumor-bearing period and exerted a synergistic antitumor effect with bimagrumab (Fig. 8c–f, Supplementary Fig. 6c–e). Thus, our results suggest a promising therapeutic strategy for pancreatic cancer patients with concomitant diabetes.

Discussion

It is well known that diabetes promotes premature cellular senescence in multiple organs and tissues, including pancreatic islets, adipose tissue, and the cardiovascular system[29–33]. However, evidence linking diabetes to senescence induction within the tumor microenvironment remains limited. In this study, we demonstrate that diabetes reshapes the tumor endothelial niche by accelerating endothelial cell senescence. A reported transcriptomic pancancer signature based on tumor endothelial senescence has been shown to predict prognosis and immunotherapy response[46]. Senescent endothelial cells exhibit disrupted cell–cell contacts, facilitating cancer cell transendothelial migration. Furthermore, multiple SASP factors contribute to tumor progression and the formation of "chemoresistant" or "premetastatic" niches[28,47–50]. Thus, senescent endothelial cells significantly influence tumor growth and metastasis. In addition to diabetes, other TEC senescence inducers include chemotherapeutic agents (e.g., doxorubicin), the VEGFR inhibitor sunitinib, reactive oxygen species, and ionizing radiation[28,47–50]. Consequently, our findings may offer therapeutic strategies for PDAC patients with diabetes and warrant further investigation into strategies targeting senescence to increase the efficacy of antitumor therapy. Given that senescent TECs are expected to present cell cycle arrest, a contradiction arises regarding increased numbers of senescent TECs in highly angiogenic microenvironments. It has been proposed that cell proliferation drives cumulative epigenetic aging and senescence onset[51]. We speculate that angiogenesis and TEC senescence occur concurrently in diabetic tumor microenvironments. Additionally, endothelial cells act as primary responders to metabolic dysregulation in tumors. Diabetes enhances fatty acid metabolism and oxidation in TECs, potentially inducing oxidative stress, which we identified as contributing to TEC senescence. An important consideration is that current senolytic approaches achieve only systemic senescence clearance. Studies have demonstrated that eliminating senescent tumor cells, CAFs, macrophages, and endothelial cells induces tumor regression[22–25,52–56]. However, these studies neither isolated the effects of specific senescent cell types nor clarified the contribution of systemic senolysis to tumor regression, as targeted elimination remains technically challenging. Future development of

https://doi.org/10.1038/s41467-025-63801-8

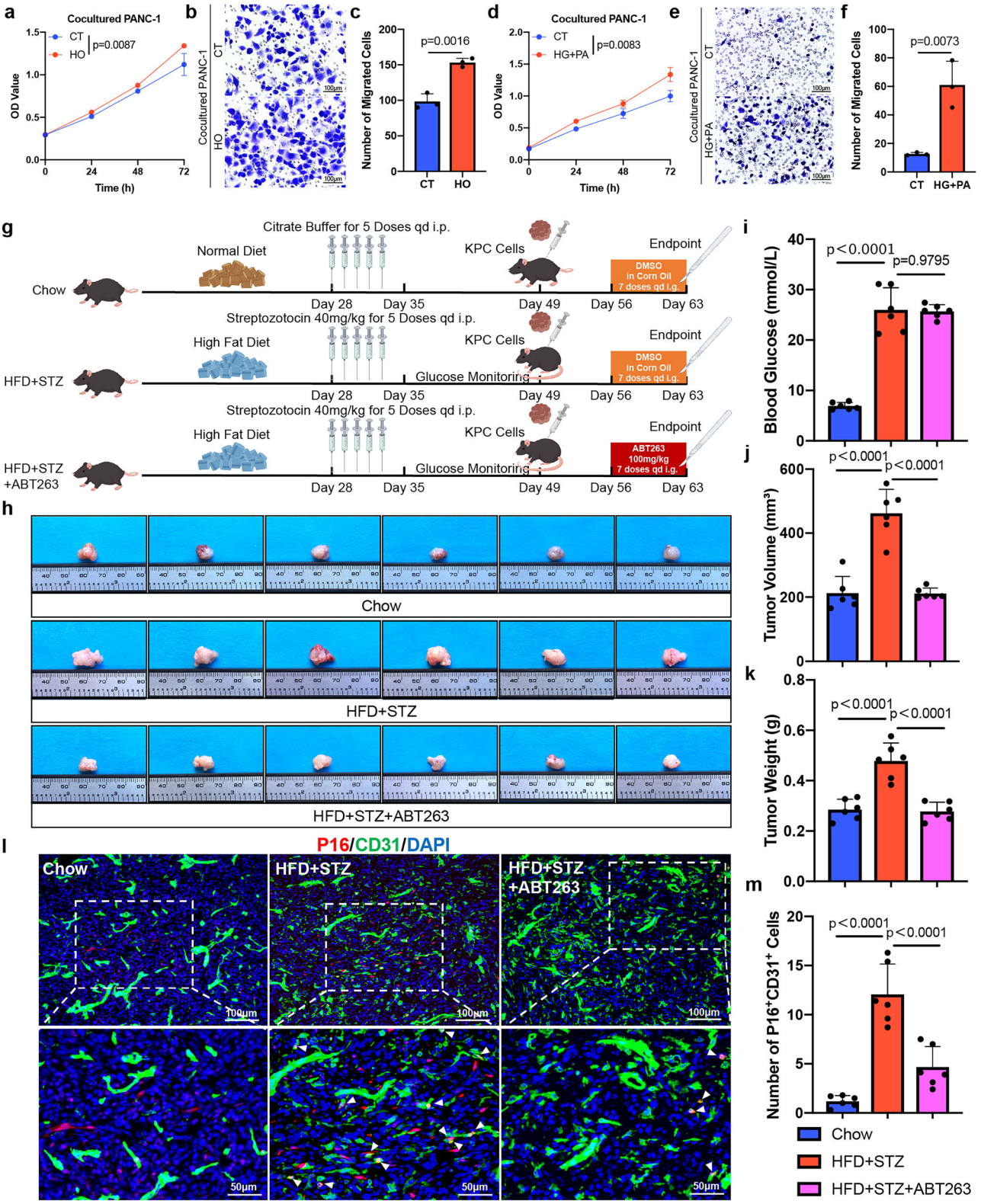

cell type-specific senolytics could help elucidate the role of discrete senescent populations in tumor progression more effectively.

Our previous study demonstrated that Notch signaling regulates liver sinusoidal endothelial cell senescence and plays a crucial role in liver regeneration[42]. Accordingly, we observed enrichment of the Notch signaling pathway in senescent TEC clusters and its activation across multiple senescent endothelial cell models. Notch activation in endothelial cells also induced senescence[43]. Collectively, these findings establish a correlation between Notch signaling and endothelial cell senescence. Our data further indicate that Notch signaling regulates the protumoral effects of senescent TECs. Notably, Notch signaling also has important regulatory functions in normal physiological processes[57]. Therefore, screening for downstream SASP factors regulated by Notch signaling could identify therapeutic targets for diabetes-associated pancreatic cancer.

Fig. 4 | Senescent endothelial cells support tumor progression. a Line graph showing OD values from CCK-8 proliferation assays for PANC-1 cells cocultured with control HUVECs or HUVECs with hydrogen peroxide (HO, 300 μM)-induced senescence ($n = 3$ biologically independent samples per group). **b**, **c** Representative images (**b**) and quantification (**c**) of the number of migrated PANC-1 cells cocultured with control HUVECs or HUVECs with HO-induced senescence in Transwell migration assays ($n = 3$ biologically independent samples per group). **d** Line graph showing OD values from CCK-8 proliferation assays for PANC-1 cells cocultured with control HUVECs or HUVECs with senescence induced by high glucose (HG, 25 mmol/L) + palmitic acid (PA, 300 μmol/L) ($n = 3$ biologically independent samples per group); low glucose (5.5 mmol/L) + BSA served as the control. **e**, **f** Representative images (**e**) and quantification (**f**) of the number of migrated PANC-1 cells cocultured with control HUVECs or HUVECs with HG + PA-induced senescence in Transwell migration assays ($n = 3$ biologically independent samples per group). **g** Schematic representation of ABT-263 treatment in KPC tumor-bearing mice (by figdraw.com). **h** Photographs of orthotopic pancreatic tumors from the chow, HFD + STZ, and HFD + STZ + ABT263 groups ($n = 6$ mice per group). **i** Bar graph showing fasting blood glucose levels in the chow, HFD + STZ, and HFD + STZ + ABT263 groups ($n = 6$ mice per group). **j** Bar graph showing tumor volumes in the chow, HFD + STZ, and HFD + STZ + ABT263 groups ($n = 6$ mice per group). **k** Bar graph showing tumor weights in the chow, HFD + STZ, and HFD + STZ + ABT263 groups ($n = 6$ mice per group). **l**, **m** Representative images (**l**) and quantification (**m**) of immunofluorescence staining for P16 (red) and CD31 (green) in chow, HFD + STZ, and HFD + STZ + ABT263 tumor tissues ($n = 6$ mice per group). The bars represent the means ± SDs. OD optical density, CT control. *P*-values were determined by two-way ANOVA (**a**, **d**), two-tailed unpaired *t*-test (**c**, **f**), and one-way ANOVA (**i**, **j**, **k**, **m**). Source data are provided as a Source Data file.

Based on the results of the bioinformatic analysis, we identified INHBB as a potential SASP factor that is specifically expressed in senescent TECs. Recent studies have indicated that INHBB participates in tumorigenesis in breast, gastric, hepatocellular, and prostate carcinomas[58]. Beyond primary solid tumors, INHBB is upregulated in endothelial cells within premetastatic niches, facilitating metastasis[59]. Through cell–cell crosstalk network analysis, we found that bimagrumab, a recombinant monoclonal antibody, can target activin type II receptors to mediate INHBB downstream signaling. Bimagrumab has demonstrated safety and efficacy in treating excess adiposity and metabolic disturbances in adults with obesity and type 2 diabetes in clinical trials[45,60]. Patients receiving bimagrumab exhibited increased lean mass, decreased body fat, and significantly improved glycemic control. Additionally, in cancer therapy, bimagrumab effectively counteracted cachexia in non-small cell lung and pancreatic cancer models[61]. However, it did not affect primary tumor progression in colon cancer models[62]. Similarly, in our tumor-bearing models, bimagrumab lacked therapeutic efficacy in nondiabetic mice but significantly suppressed tumor growth in diabetic mice. Short-term bimagrumab monotherapy did not significantly reduce fasting blood glucose levels in diabetic tumor-bearing mice. Their limited survival time restricted the observation of the long-term effects of bimagrumab treatment, yet combination therapy with metformin resulted in synergistic antitumor activity and attenuated hyperglycemia progression. These results suggest the need for further investigation of long-term outcomes in genetically engineered PDAC models. Another question is why bimagrumab lacks antitumor effects in nondiabetic mice. As INHBB is an endothelium-specific factor with low expression in nondiabetic tumors, the observed effects of bimagrumab in such models are confined to cachexia[62,63]. These findings further substantiate INHBB as a metabolic disorder-responsive factor in diabetes. In particular, pancreatic cancer is closely associated with metabolic dysregulation. Our findings highlight the potential of bimagrumab as a precise pharmacologic intervention for pancreatic cancer patients with concomitant diabetes. Consequently, we will further perform scRNA-seq to identify which cell populations (including TECs) are altered by bimagrumab in diabetic models. Clinical studies are warranted to evaluate its translational value in diabetic pancreatic cancer patients.

This study has several limitations. First, whether diabetes affects tumorigenesis, including early pancreatic intraepithelial neoplasia (PanIN) lesions, was not investigated and requires elucidation using genetically engineered mouse models (GEMMs). Second, the effects of long-term bimagrumab treatment on diabetic pancreatic tumor regression and metabolic improvement remain uncharacterized. Third, while senescent endothelial cells only slightly promoted pancreatic cancer cell proliferation in vitro, they significantly accelerated tumor progression in vivo. We propose that in vivo malignant behavior involves multifactorial influences that cannot be fully extrapolated from in vitro results. Enhanced migratory capacity may also drive tumor growth through increased invasion potential. Additionally, as INHBB belongs to the TGF-β superfamily, it may induce epithelial-to-mesenchymal transition, angiogenesis, fibrosis, and cancer-associated fibroblast (CAF) activation to promote tumor progression[59,64]. These mechanisms warrant further investigation. Finally, elimination of systemic senescent cells may impair normal physiological processes[40], representing a major therapeutic constraint that limits clinical translation. Therefore, we targeted a specific SASP factor in senescent tumor endothelial cells for translational research, indirectly supporting our findings. As noted previously, developing future methods for specific senescent cell elimination would better elucidate the role of senescent TECs in tumor progression.

Methods

Patients

To investigate whether a history of diabetes is associated with the prognosis of primary pancreatic ductal adenocarcinoma, we retrospectively analyzed the clinicopathological and follow-up data of patients with resectable primary pancreatic cancer treated from 2015 to 2020 at the Department of Hepatobiliary Surgery, Xijing Hospital (Xi'an, China). The inclusion criteria were as follows: ① pathologically confirmed pancreatic ductal adenocarcinoma following surgical resection; ② absence of distant metastasis; ③ primary tumors deemed resectable through pre- and intraoperative evaluation; ④ documented records pertaining to diabetes history; and ⑤ complete pathological records. The exclusion criteria were as follows: ① metastatic disease at diagnosis (e.g., liver metastasis); ② unresectable tumors due to poor physiological status or vascular invasion precluding resection or reconstruction (e.g., celiac trunk, superior mesenteric artery or portal vein involvement); ③ missing diabetes history records; ④ absence of pathological documentation; and ⑤ lack of postoperative follow-up. Informed consent was obtained from all participants and included a statement on the clinicopathological data for scientific research, with no financial compensation provided. Sex was determined through self-reports. Ethics approval was granted by the Medical Ethics Committee of Xijing Hospital (approval number: KY20243015-1; 5 March 2024).

Publicly available clinical and survival data for PDAC patients were collected from the cBioPortal database (http://www.cbioportal.org/) using the MSK-IMPACT pancreatic cancer cohort. The inclusion criteria were as follows: ① histologically confirmed pancreatic ductal adenocarcinoma with follow-up records; ② nonmetastatic disease; ③ documented records pertaining to diabetes history; and ④ primary resectable tumors. The exclusion criteria were as follows: ① metastatic malignancies; ② missing diabetes history documentation; ③ locally advanced tumors; and ④ incomplete follow-up records.

Animals

Specific-pathogen-free (SPF) male C57BL/6J mice (strain #N00010), aged 8 weeks, were purchased from Beijing Vital River Laboratory

https://doi.org/10.1038/s41467-025-63801-8

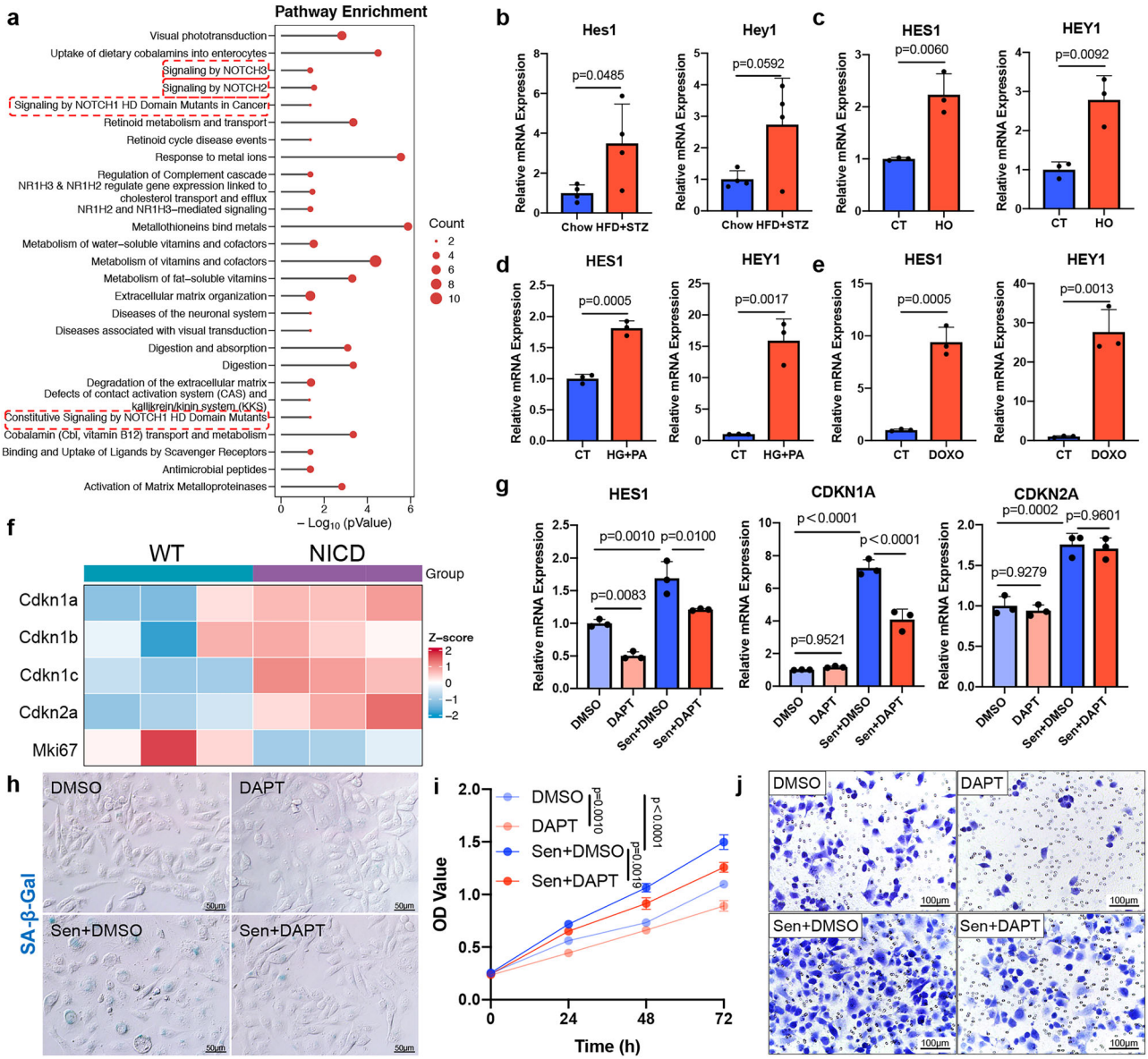

Fig. 5 | Notch signaling is activated in senescent endothelial cells. a Bubble plot showing pathway enrichment analysis for specific markers of senescent capillary endothelial cells ($n = 14$ patients in the control group and $n = 10$ patients in the diabetic group). **b** Bar graph showing the mRNA expression of Hes1 and Hey1 in TECs isolated from KPC tumors in chow and HFD + STZ mice ($n = 4$ mice per group). **c** Bar graph showing the mRNA expression of HES1 and HEY1 in HUVECs with senescence induced by hydrogen peroxide (HO, 300 μM) ($n = 3$ biologically independent samples per group). **d** Bar graph showing the mRNA expression of HES1 and HEY1 in HUVECs with senescence induced by HG + PA ($n = 3$ biologically independent samples per group). **e** Bar graph showing the mRNA expression of HES1 and HEY1 in HUVECs with senescence induced by doxorubicin ($n = 3$ biologically independent samples per group). **f** Heatmap showing the expression of senescence-related genes in NICD-overexpressing TECs based on RNA-seq data from the GEO database (GSE111127; $n = 3$ mice per group). **g** Bar graph showing the mRNA expression of HES1, CDKN1A, and CDKN2A in proliferating or senescent HUVECs treated with DMSO or DAPT ($n = 3$ biologically independent samples per group). **h** Representative images of SA-β-galactosidase (SA-β-Gal) staining (blue) in proliferating or senescent HUVECs treated with DMSO or DAPT ($n = 3$ biologically independent samples per group). **i** Line graph showing OD values from CCK-8 proliferation assays of PANC-1 cells cocultured with proliferating or senescent HUVECs treated with DMSO or DAPT ($n = 3$ biologically independent samples per group). **j** Representative images from Transwell migration assays for PANC-1 cells cocultured with proliferating or senescent HUVECs treated with DMSO or DAPT ($n = 3$ biologically independent samples per group). OD optical density, WT wild type, TEC tumor endothelial cell, HO hydrogen peroxide, HG high glucose, PA palmitic acid, DMSO dimethyl sulfoxide. The bars represent the means ± SDs. *P*-values were determined by a two-sided hypergeometric test with Benjamini–Hochberg correction (**a**), two-tailed unpaired *t*-test (**b**–**e**), and two-way ANOVA (**g**, **i**). Source data are provided as a Source Data file.

Animal Technology Co., Ltd. RBPJ^{ECKO} mice (CDH5-Cre^{ERT}; RBPJ$^{flox/flox}$) on a C57BL/6J background were generated and validated as previously described[65]. To induce Cre-mediated recombination, 6-week-old male RBPJ^{ECKO} mice received daily intraperitoneal injections of tamoxifen (100 mg/kg; Sigma–Aldrich, St. Louis, MO) for five consecutive days. All animal procedures were approved by the Animal Ethics Committee of the Fourth Military Medical University.

Diabetic models

To observe tumor progression in vivo, we established four mouse models representing different diabetes stages on a C57BL/6J background: ① The chow group: 8-week-old male C57BL/6J mice received a normal diet for 4 weeks, followed by intraperitoneal injection of citrate buffer (49.5% 0.1 M citric acid monohydrate, 60347ES25, Yeasen; 50.5% 0.1 M trisodium citrate dihydrate, 60348ES25, Yeasen) for 5

https://doi.org/10.1038/s41467-025-63801-8

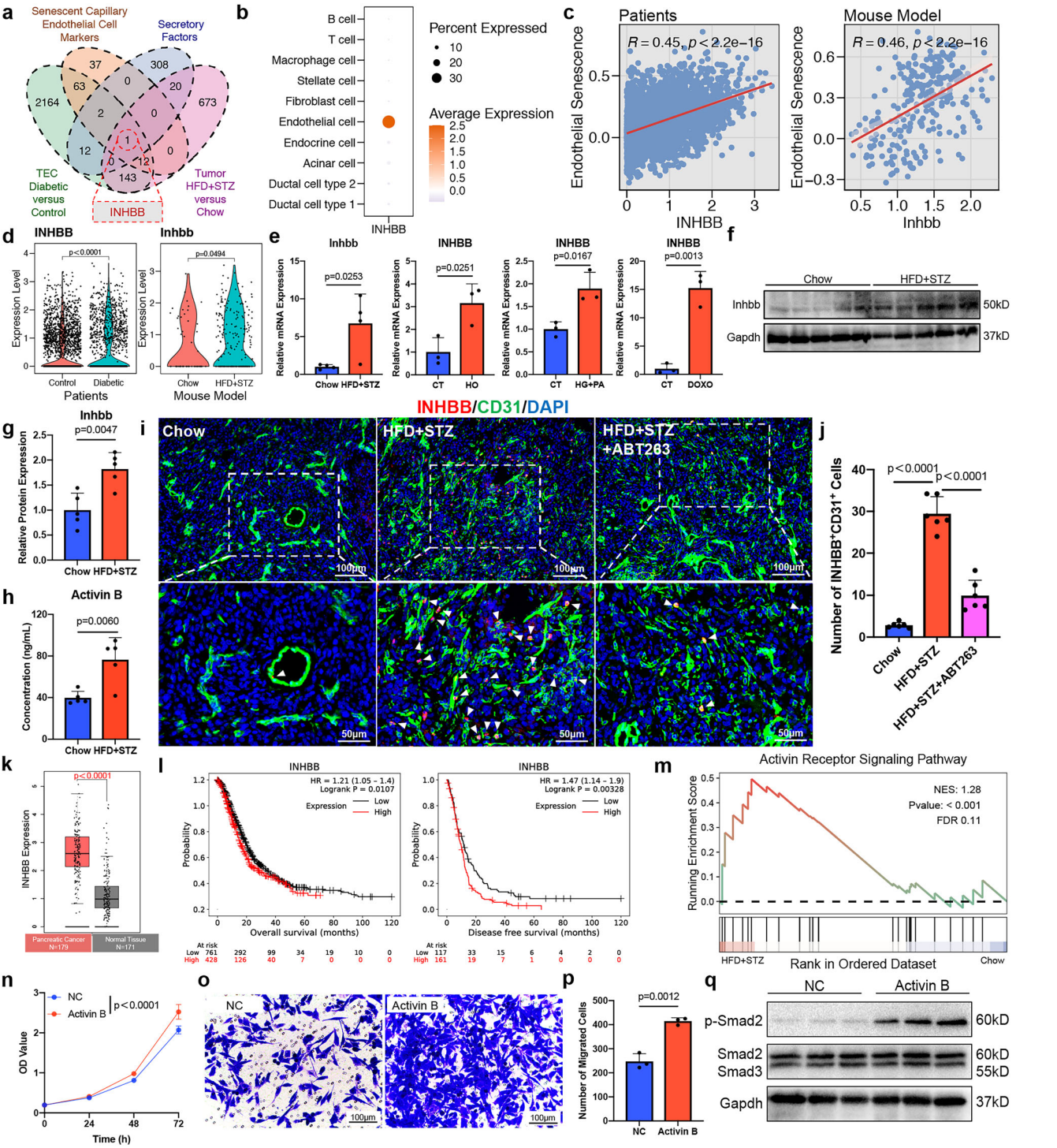

consecutive days. ② The 4-week HFD group: Mice were fed a high-fat diet (HFD; D12492, Research Diets, 60% fat) for 4 weeks and then received citrate buffer injections as described above. ③ The 16-week HFD group: Mice were fed a HFD for 16 weeks to serve as a prediabetic or early-stage diabetic model characterized by impaired glucose tolerance and mild fasting hyperglycemia. ④ The HFD + STZ group: Mice were fed a HFD for 4 weeks, followed by intraperitoneal injection of streptozotocin (40 mg/kg; S0130; Sigma–Aldrich) for 5 consecutive days, after which type 2 diabetes with significant fasting hyperglycemia and impaired glucose tolerance was induced. Ten days after injection, fasting blood glucose levels were measured after a 10-h fast. Intraperitoneal glucose tolerance tests (IPGTTs) were used to assess glucose tolerance. Diabetic mice were defined as those with a fasting glucose concentration ≥11.1 mmol/L and impaired glucose tolerance. To exclude direct effects of STZ on tumors, HFD + STZ mice received insulin glargine (5 IU/kg, subcutaneous injection, Sanofi-Aventis) every 12 h. Prefasting blood glucose levels were measured 10 h after insulin injection to prevent hypoglycemia-related mortality.

Orthotopic pancreatic cancer models

Two weeks after STZ or citrate buffer injection, 3×10^5 KPC cells or 1×10^6 Pan02 cells were orthotopically injected into the pancreatic capsule. Tumor-bearing mice were euthanized 14 days after inoculation. For $RBPJ^{ECKO}$ and control ($CDH5\text{-}Cre^{ERT}$-negative; $RBPJ^{flox/flox}$) mice,

Fig. 6 | INHBB is a potential SASP factor. a Venn diagram for intersection analysis. **b** Dot plot showing INHBB expression in the pancreatic cancer microenvironment. **c** Scatter plots showing the correlation between INHBB expression and the endothelial senescence scores. **d** Violin plot showing INHBB expression in TECs from nondiabetic and diabetic tumors. **e** Bar graphs showing INHBB mRNA expression in TECs isolated from KPC tumors and different senescent endothelial cell models. **f**, **g** Representative images (**f**) and quantification (**g**) of INHBB protein expression in chow and HFD + STZ tumors. **h** Bar graphs showing the Activin B concentration in tumor homogenates. **i**, **j** Representative images (**i**) and quantification (**j**) of immunofluorescence staining for INHBB (red) and CD31 (green) in chow, HFD + STZ, and HFD + STZ + ABT263 tumors. **k** Box plot showing INHBB expression in pancreatic tumors ($n = 179$ patients) and normal pancreas ($n = 171$ patients). The data are presented as medians and quartiles; the box bounds represent the upper and lower quartiles. **l** Kaplan–Meier survival curves for overall survival ($n = 761$ with low and $n = 428$ with high INHBB expression) and disease-free survival ($n = 117$ with low and $n = 161$ with high INHBB expression) in pancreatic cancer patients. **m** Gene set enrichment analysis for the Activin receptor signaling pathway. **n** Line graph showing OD values from CCK-8 assays for Activin B- or vehicle-treated Pan02 cells. **o**, **p** Representative images (**o**) and quantification (**p**) of migrated Pan02 cells treated with Activin B or vehicle. **q** Phosphorylated and total Smad2 levels in Activin B- or vehicle-treated Pan02 cells. NC negative control, TEC tumor endothelial cell, OD optical density. The bars represent the means ± SDs. **a**–**d**, **m** $n = 3$ mice per group for bulk RNA-seq; $n = 14$ patients in the control group and $n = 10$ patients in the diabetic group for scRNA-Seq; $n = 2$ mice in the chow group and $n = 4$ mice in the HFD + STZ group for scRNA-seq. **e**–**j**, $n = 4$–6 mice per group. **e**, **n**–**q** $n = 3$–6 biologically independent samples per group. *P*-values were determined by the Spearman test (**c**), Mann–Whitney test (**d**), two-tailed unpaired *t*-test (**e**, **g**, **h**, **p**), log-rank test (**l**), one-way (**j**) and two-way ANOVA (**n**). Source data are provided as a Source Data file.

2×10^6 Pan02 cells were injected into the pancreatic capsule of 8-week-old male mice. These tumor-bearing mice were euthanized 21 days after injection. The tumor dimensions were measured using calipers. The tumor volume was calculated as 1/2 (length × width × height). Humane endpoints were defined as follows: ① >20% body weight loss relative to the initial inoculation weight; ② marked abdominal distension/ascites; ③ significant reduction in food and water intake; and ④ persistent painful tremors or a hunched posture. All animal experiments were performed in accordance with the Guide for the Care and Use of Laboratory Animals prepared by the National Academy of Science. All animal work was approved by the Animal Experiment Administration Committee of Fourth Military Medical University (Xi'an, China). The maximal permitted tumor volume (2000 mm^3) was not exceeded in any experiment.

Cell lines

Pan02 cells, HUVECs, and PANC-1 cells were purchased from the American Type Culture Collection (ATCC). KPC cells (cat. no. NM-YD04) were purchased from Shanghai Model Organisms Center, Inc. The cell lines were cultured in DMEM (Gibco) supplemented with 10% fetal bovine serum (FBS) and 1% penicillin/streptomycin solution (P/S). To induce senescence, HUVECs were treated with hydrogen peroxide (HO, 300 μM) for 24 h or with high glucose (HG, 25 mmol/L) and palmitic acid (PA, 300 μmol/L) for 48 h.

Single-cell RNA-Seq data processing

To perform scRNA-seq analysis on the pancreatic cancer model, cell suspensions derived from pancreatic tumors of chow ($n = 2$) and HFD + STZ ($n = 4$) mice were processed using the 10× Chromium System (10× Genomics, USA) according to the manufacturer's protocol. Complementary DNA (cDNA) library construction and scRNA-seq data processing were performed by Gene Denovo (Guangzhou, China). The Seurat package (version 5.1.0) in R software (version 4.2.3) was used for quality control and downstream analysis. Batch effects were corrected using the Harmony package (version 0.1.1). The top 2000 variable genes were identified using the FindVariableFeatures function. Data were subsequently normalized (NormalizeData function), scaled, and centered (ScaleData function) based on these variable genes. After principal component analysis (RunPCA function) was performed, the RunHarmony function was used to reduce batch effects within the integrated scRNA-seq data across samples. The top 20 harmony dimensions were then used for unsupervised clustering in Seurat. Doublets were removed using the DoubletFinder package (version 2.0.4). Major cell types in the tumor microenvironment were identified using specific markers from the CellMarker 2.0 database (bio-bigdata.hrbmu.edu.cn/CellMarker).

scRNA-seq data for clinical pancreatic cancer patients were also obtained from the Genome Sequence Archive (GSA) database (accession number CRA001160, ngdc.cncb.ac.cn). To address batch effects, the Harmony package was applied as described above. Cell type annotations and clinical feature data can be downloaded from the CRA001160 dataset. Cell markers for each cell type were obtained from the published article associated with this dataset[36]. Since correlation analysis can be strongly influenced by an excess of zero counts (dropout events), we utilized the scImpute package (version 0.0.9) to accurately and robustly impute dropout values in the scRNA-seq data prior to correlation analysis[66].

Endothelial cell subtype analysis

To further investigate endothelial cell heterogeneity in pancreatic cancer patients with or without diabetes, endothelial cell subsets were extracted and subjected to unsupervised clustering. Based on published literature[37], the AddModuleScore function in the Seurat package was utilized to calculate enrichment scores for arterial, venous, and capillary endothelial cell phenotypes using highly expressed markers, enabling the annotation of endothelial subtypes. To further evaluate cell proliferation and senescence status, enrichment scores were calculated using markers associated with the pancancer endothelial senescence signature[46], endothelial proliferation (GOBP: POSITIVE REGULATION OF ENDOTHELIAL CELL PROLIFERATION; GO:0001938), endothelial apoptosis (GOBP: POSITIVE REGULATION OF ENDOTHELIAL CELL APOPTOTIC PROCESS; GO:2000353), fatty acid metabolism (REACTOME: FATTY ACID METABOLISM; R-HSA-8978868), fatty acid oxidation (GOBP: POSITIVE REGULATION OF FATTY ACID OXIDATION; GO:0046321), and Notch signaling (GOBP: POSITIVE REGULATION OF NOTCH SIGNALING PATHWAY; GO:0045747) phenotypes.

Cell–cell crosstalk network analysis

To investigate cell crosstalk between different endothelial subtypes and pancreatic cancer cells, the CellChat package (version 1.6.1) was used. Ligand–receptor pairs with *P*-values < 0.05 (calculated via a one-sided permutation test in CellChat) were deemed to have significant interactions between the subpopulations. Potential crosstalk networks between endothelial subtypes and malignant cells were visualized using dot plots.

Bulk RNA-seq analysis

RNA extraction, sequencing and analysis were performed by Gene Denovo (Guangzhou, China) using an Illumina HiSeq3000 system (Illumina, San Diego, CA). Briefly, pancreatic tumor tissues were collected from chow or HFD + STZ mice ($n = 3$ per group). After the capsule and overlying tissues were removed, the tissues were washed with PBS. Total RNA was isolated using TRIzol (Invitrogen) following the manufacturer's protocol. Bulk RNA-seq data from LFD and HFD KPC models were obtained from the Gene Expression Omnibus (GSE266899; www.ncbi.nlm.nih.gov/geo/). Principal component analysis (PCA; stats package version 4.2.3, prcomp function) was performed for dimensionality reduction and sample relationship visualization. Endothelial disorganization-associated genes included

https://doi.org/10.1038/s41467-025-63801-8

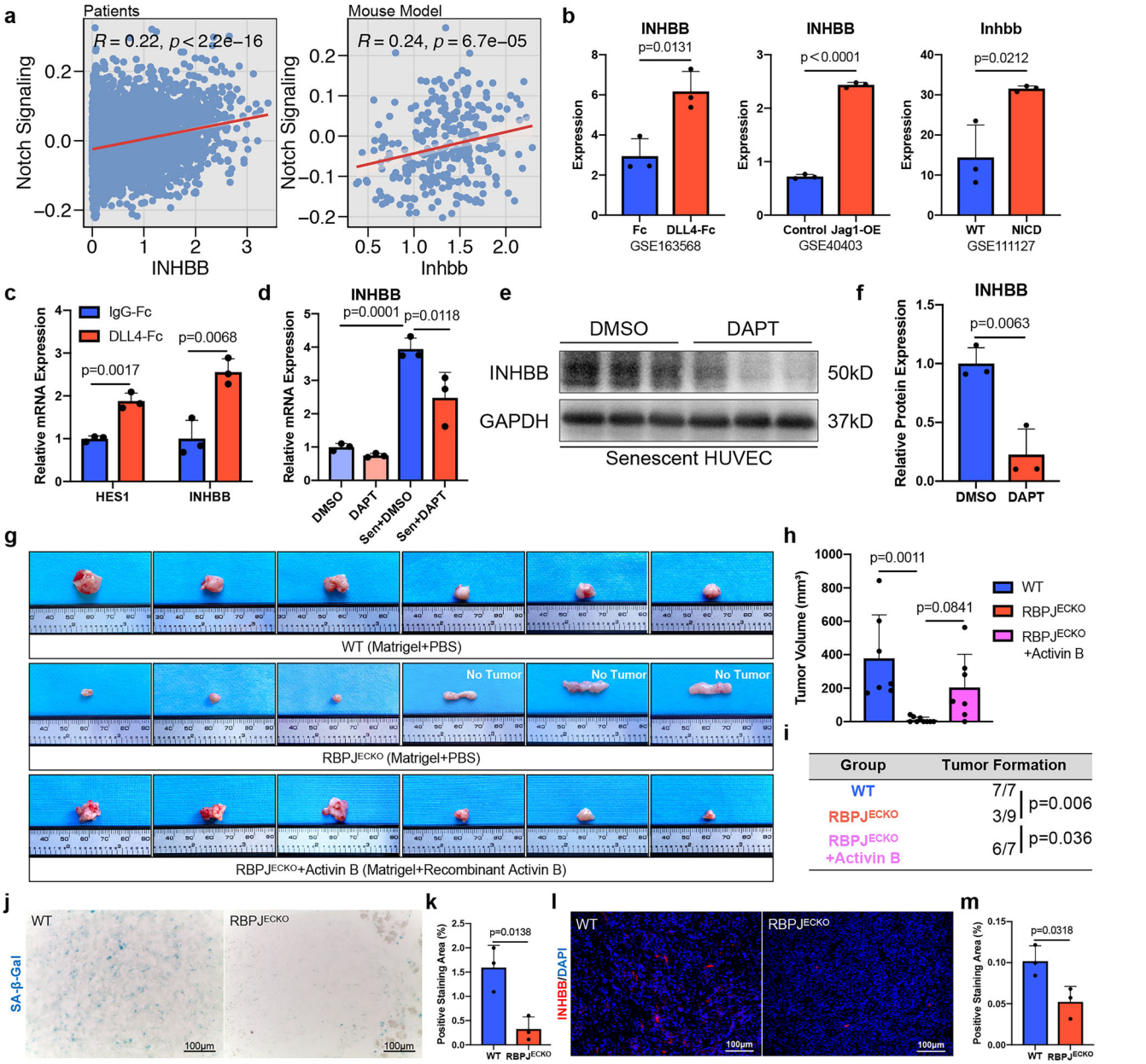

Fig. 7 | Notch signaling regulates the expression of INHBB. a Correlation scatter plots showing the correlation between INHBB expression and the Notch signaling score in tumor endothelial cells based on scRNA-seq data of PDAC patients ($n = 14$ patients in the control group and $n = 10$ patients in the diabetic group) and tumor-bearing mice ($n = 2$ mice in the chow group and $n = 4$ mice in the HFD + STZ group). **b** Bar graphs showing INHBB expression in Notch-activated HUVECs and TECs according to the bulk RNA-seq data in the GEO database (GSE163568, GSE40403, and GSE111127; $n = 3$ biologically independent samples per group). **c** Bar graphs showing the mRNA expression of HES1 and INHBB in Notch-activated HUVECs treated with recombinant DLL4-Fc protein ($n = 3$ biologically independent samples per group). **d** Bar graph showing the mRNA expression of INHBB in proliferating and senescent HUVECs treated with DMSO or 10 μM DAPT ($n = 3$ biologically independent samples per group). **e**, **f** Representative images (**e**) and quantification (**f**) of INHBB protein expression in senescent HUVECs treated with DMSO or 10 μM DAPT detected by Western blotting ($n = 3$ biologically independent samples per group). **g** Tumor samples from CDH5-Cre^{ERT}-negative; RBPJ$^{flox/flox}$ mice (WT, $n = 7$ mice), CDH5-Cre^{ERT}; RBPJ$^{flox/flox}$ mice (RBPJ^{ECKO}, $n = 9$ mice) and recombinant Activin B coinjected RBPJ^{ECKO} mice ($n = 7$ mice). **h** Bar graph showing tumor volumes in the WT ($n = 7$ mice), RBPJ^{ECKO} ($n = 9$ mice), and RBPJ^{ECKO}+Activin B ($n = 7$ mice) groups. **i** Table for tumor formation ratios in the WT ($n = 7$ mice), RBPJ^{ECKO} ($n = 9$ mice), and RBPJ^{ECKO}+Activin B groups ($n = 7$ mice). **j**, **k** Representative images (**j**) and quantification (**k**) of SA-β-Gal staining (blue) in tumor tissues collected from WT and RBPJ^{ECKO} mice ($n = 3$ mice per group). **l**, **m** Representative images (**l**) and quantification (**m**) of INHBB staining (red) in tumor tissues collected from WT and RBPJ^{ECKO} mice ($n = 3$ mice per group). The bars represent the means ± SDs. *P*-values were determined by the Spearman test (**a**), two-tailed unpaired *t*-test (**b**, **c**, **f**, **k**, **m**), two-way ANOVA (**d**), one-way ANOVA (**h**) and chi-square test (**i**). Source data are provided as a Source Data file.

Fabp4, Igfbp7, Sparc, Sparcl1, Col4a1, Cd81, Col4a2, Igfbp3, Fabp5, Tshz2, Rgcc, S100a6, Vwa1, Ebf1, Tmem252, Gapdh, Pdlim1 and Prnp[34].

Differentially expressed gene analysis and pathway enrichment
From the scRNA-seq data, cluster-specific marker genes for each endothelial subtype were identified using the FindAllMarkers function in the Seurat package based on normalized expression data. Differentially expressed genes (DEGs) between endothelial cells in the control and diabetic groups were identified with the FindMarkers function. With respect to the bulk RNA-seq data, DEGs between the control and diabetic groups were identified using the DESeq2 package (version 1.38.3). Statistical significance was

https://doi.org/10.1038/s41467-025-63801-8

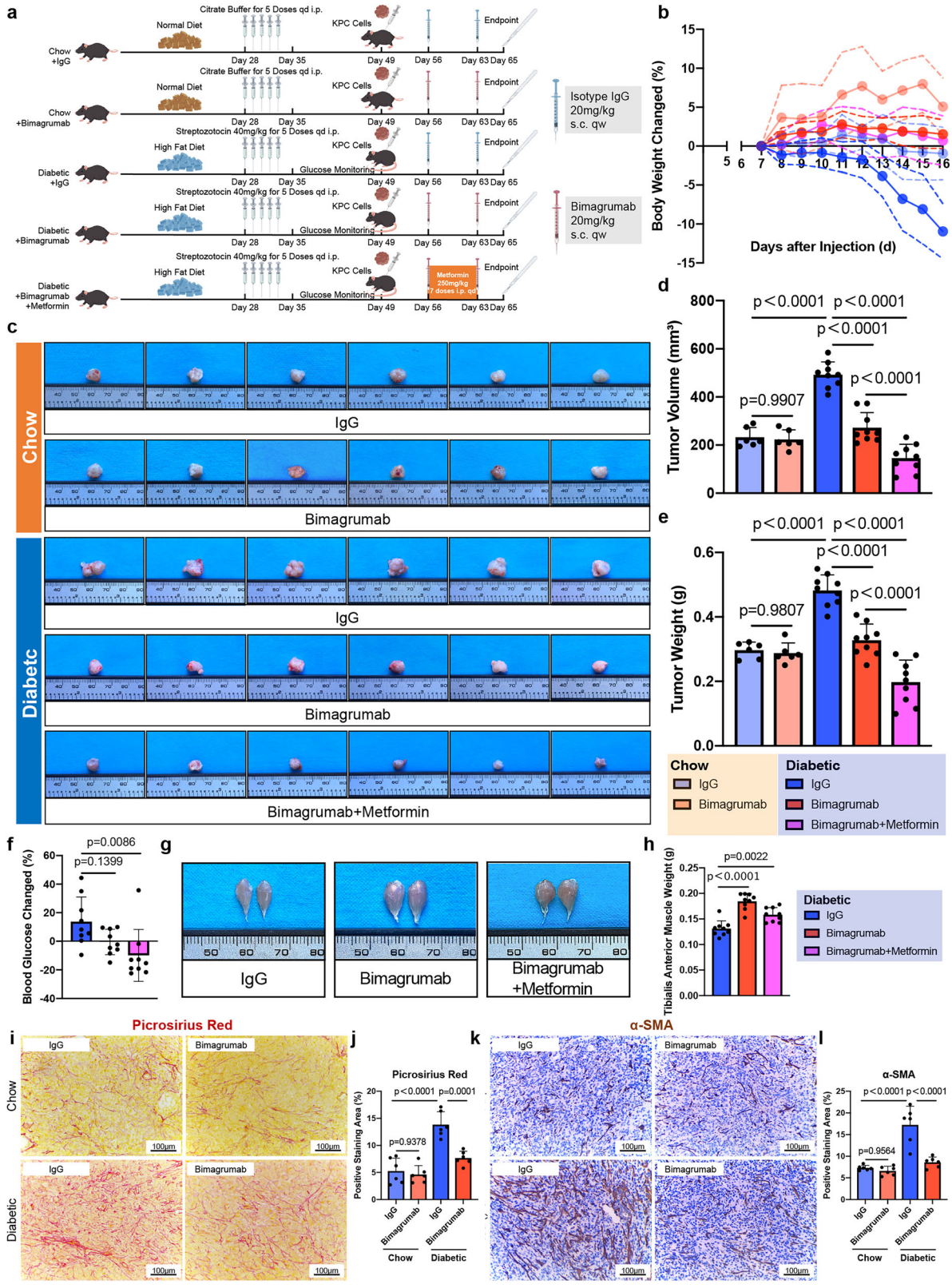

assessed by the Wilcoxon test, and the Benjamini–Hochberg correction was used to adjust the *P*-values. FDR < 0.05 was the cutoff criterion for differentially expressed genes. Pathway enrichment was performed using the enrichPathway function in the clusterProfiler package (version 4.6.2) via two-sided hypergeometric testing with FDR correction.

Flow cytometry

To determine the ratio of senescent endothelial cells in the tumor microenvironment, flow cytometry was used to compare the abundance of $CD45^-CD31^+SA\text{-}\beta\text{-}Gal^+$ cells between the chow and HFD + STZ groups. After the tumor cell suspensions were prepared, the Fc receptors were blocked with TruStain FcX™ antibody (BioLegend,

Fig. 8 | Bimagrumab inhibits tumor progression in diabetic mice. a Schematic representation of bimagrumab treatment in chow and diabetic KPC tumor-bearing mice (by figdraw.com). **b** Line graph showing body weight changes in chow ($n = 6$ mice per group) and diabetic ($n = 9$ mice per group) KPC tumor-bearing mice treated with IgG, bimagrumab, or bimagrumab+metformin. **c** Pancreatic tumor samples from chow ($n = 6$ mice per group) and diabetic ($n = 9$ mice per group) KPC tumor-bearing mice treated with IgG, bimagrumab, or bimagrumab+metformin. **d** Bar graph showing tumor volumes in chow ($n = 6$ mice per group) and diabetic ($n = 9$ mice per group) KPC tumor-bearing mice treated with IgG, bimagrumab, or bimagrumab+metformin. **e** Bar graph showing tumor weights in chow ($n = 6$ mice per group) and diabetic ($n = 9$ mice per group) KPC tumor-bearing mice treated with IgG, bimagrumab, or bimagrumab+metformin. **f** Bar graph showing fasting blood glucose changes in diabetic tumor-bearing mice after treatment with 2 doses of IgG, 2 doses of bimagrumab alone, or 2 doses of bimagrumab combined with 7 doses of metformin ($n = 9$ mice per group). **g** Representative images of bilateral tibialis anterior muscles from diabetic mice treated with IgG, bimagrumab, or bimagrumab+metformin ($n = 9$ mice per group). **h** Bar graph showing the weights of the bilateral tibialis anterior muscles in diabetic mice ($n = 9$ mice per group). **i**, **j** Representative images (**i**) and quantification (**j**) of picrosirius red staining (red) in tumors from chow and diabetic KPC tumor-bearing mice treated with IgG or bimagrumab ($n = 6$ mice per group). **k**, **l** Representative images (**k**) and quantification (**l**) of α-SMA staining (brown) in tumors from chow and diabetic KPC tumor-bearing mice treated with IgG or bimagrumab ($n = 6$ mice per group). The bars represent the means ± SDs. *P*-values were determined by one-way ANOVA (**d**–**f**, **h**) and two-way ANOVA (**j**, **l**). The effects of bimagrumab in the chow and diabetic groups were also assessed by two-way ANOVA (**d**, **e**). Source data are provided as a Source Data file.

101319), and the cells were incubated with a PE-conjugated anti-mouse CD31 (PECAM-1) antibody (BioLegend, 160203) and a Pacific blue-conjugated anti-mouse CD45 (PTPRC) antibody (BioLegend, 157211) for 30 min at 4 °C. Cell suspensions were washed with PBS containing 1% BSA, and the cells were resuspended in 100 μL of fixation solution (2% paraformaldehyde, PFA). The cells were incubated for 10 min at room temperature in the dark. The cells were then washed in PBS containing 1% BSA to remove the fixation solution. The cells were resuspended in 100 μL of the working solution of the CellEvent™ Senescence Green Flow Cytometry Assay Kit (Invitrogen™, C10841, 1:1000) and incubated for 90 min at 37 °C in the dark. The cells were finally washed with PBS containing 1% BSA and resuspended for flow cytometry analysis. The gating strategy is shown in Supplementary Fig. 2i. The antibodies used are listed in Supplementary Table 3.

Primary tumor endothelial cell isolation

Orthotopic pancreatic tumors were mechanically minced and digested in 1 mg/mL collagenase IV (Sigma–Aldrich, C5138) and 100 μg/mL DNase I (Roche, 10104159001) for 25 min at 37 °C. After filtration through a 70-μm strainer, the cell suspensions were centrifuged at 350 × *g* for 5 min (4 °C). Red blood cells were lysed using lysis buffer. Approximately 2×10^7 cells were resuspended in 100 μL of MACS buffer containing 10 μL of anti-CD45-coated magnetic beads (Miltenyi Biotec, 130-052-301) and incubated at 4 °C for 15 min. Cells underwent negative selection with the Manual MACS Separator for CD45 depletion. $CD45^-$ cells were incubated with anti-CD31-coated magnetic beads (Miltenyi Biotec, 130-097-418) for 15 min at 4 °C. $CD31^+$ cells (TECs) were positively selected using the Manual MACS Separator. Primary TECs were plated in 24-well plates and cultured in endothelial cell medium (ScienCell, 1001) supplemented with 5% FBS, 1% endothelial cell growth supplement (ScienCell, 1052), and 1% P/S (ScienCell, 0503).

Immunofluorescence staining

Tumor tissues were embedded in optimal cutting temperature (OCT) compound (Sakura, 4583), followed by 4 h of fixation in 4% PFA and overnight dehydration in 30% sucrose. Frozen sections were air-dried at room temperature for 2 h. The sections were subsequently washed three times with PBS, blocked with immunostaining blocking buffer containing 0.3% Triton X-100 (Beyotime, P0102) for 1 h at room temperature, and incubated with primary antibodies overnight at 4 °C. After the sections were washed with PBS, they were incubated with secondary antibodies at 37 °C for 1 h, followed by nuclear staining with DAPI (Servicebio, G1012) for 10 min at room temperature. Images were acquired using a fluorescence microscope. The antibodies used are listed in Supplementary Table 3.

Immunohistochemistry staining

Tumor tissues were fixed in 4% PFA (Servicebio, G1101) and embedded in paraffin. The sections were subjected to deparaffinization, rehydration, and antigen retrieval, treated with 3% hydrogen peroxide for 25 min, and then washed three times with PBS. After blocking with 3% BSA for 30 min, the sections were incubated with primary antibodies overnight at 4 °C. Following three washes with PBS, the sections were incubated with secondary antibodies at room temperature for 60 min, washed three times with PBS, and developed with DAB substrate (the development time was microscopically optimized). The sections were counterstained with hematoxylin for 3 min, rinsed with tap water, briefly immersed in a hematoxylin differentiation solution, rinsed, treated with a hematoxylin bluing solution, and rinsed again. Images were acquired using a brightfield microscope. The antibodies used are listed in Supplementary Table 3.

Hematoxylin and eosin (H&E) staining

After deparaffinization and rehydration, sections were stained with hematoxylin for 5–10 min, rinsed briefly in distilled water, treated with hematoxylin differentiation solution, rinsed with tap water, immersed in hematoxylin bluing solution, and rinsed again. The sections were then dehydrated in 95% ethanol for 1 min and stained with eosin for 1–3 min. Images were acquired using a brightfield microscope.

Senescence-associated β-galactosidase (SA-β-gal) staining

SA-β-gal activity was assessed in tumor tissues and cultured cells using a senescence β-galactosidase staining kit (Beyotime, C0602). Cells or tissue sections were washed three times with PBS and fixed for 15 min at room temperature. After 3 washes with PBS, β-galactosidase staining solution was added (930 μL of staining solution C supplemented with 10 μL of solution A, 10 μL of solution B, and 50 μL of X-Gal; pH 6.0), and the samples were incubated overnight at 37 °C without CO_2. The samples were subsequently washed three times with PBS, and blue staining was examined by microscopy.

In vitro and in vivo coculture assays

Primary TECs were cultured in endothelial cell medium (ScienCell, 1001) for 24 h. Conditioned medium (CM) was collected and centrifuged at 2000 × *g* for 5 min (4 °C), after which the cell debris was removed. CM from TECs derived from chow or HFD + STZ mice were used to treat KPC and Pan02 cells for 24 h in vitro. For in vivo coculture, freshly isolated chow or HFD + STZ TECs were mixed with KPC or Pan02 cells at a 1:1 ratio. The mixed suspensions were injected into the pancreatic capsules of C57BL/6J mice fed a normal diet. The mice were sacrificed 14 days after inoculation. The tumor volume was calculated based on caliper measurements, as previously described.

Activin B treatment assay

To evaluate the protumoral effects of Activin B, Pan02 cells were treated with 50 ng/mL recombinant Activin B for 24 h. Proliferation and migration were assessed. Phosphorylated Smad2 levels were analyzed by Western blotting. For in vivo studies, 2×10^6 Pan02 cells in Matrigel containing 2 μg/mL Activin B were injected into the

pancreatic capsules of RBPJ^{ECKO} mice. The mice were sacrificed 21 days after injection. The tumor dimensions (length/width/height) were measured using calipers, and the tumor volume was calculated as previously described.

Cell proliferation assay
KPC, Pan02 or PANC-1 cells (2×10^3) were seeded in 96-well plates. CCK-8 assays were conducted after 0, 24, 48, and 72 h. Next, 110 μL of DMEM containing 10 μL of CCK-8 solution was added per well and incubated for 2 h (37 °C, 5% CO_2). The absorbance (450 nm) was measured using a microplate reader.

Cell migration assay
For migration assays, 4×10^4 KPC/Pan02 cells or 6×10^4 PANC-1 cells in serum-free DMEM were seeded into 8.0-μm-pore Transwell inserts (Corning, CLS3422; 6.5 mm diameter). The lower chamber contained 800 μL of DMEM supplemented with 20% FBS. After 24 h of incubation (37 °C, 5% CO_2), nonmigrated cells on the upper surface of the insert were removed using a cotton swab. The migrated cells on the lower surface were fixed in 4% PFA and stained with 1% crystal violet. Images were acquired using a brightfield microscope.

Real-time quantitative PCR assay
RNA was isolated from cells using TRIzol (Invitrogen) per the manufacturer's protocol. For cDNA synthesis, 500 ng of total RNA was reverse transcribed with M-MLV reverse transcriptase (Accurate Biology, AG11728). qPCR was performed on a Bio-Rad real-time PCR system. Gene expression was normalized to that of endogenous controls and calculated via the ΔΔCt method. The primers used are listed in Supplementary Table 4.

Western blotting
Proteins from tumors or cells were extracted in RIPA lysis buffer supplemented with protease inhibitors. The protein concentration was quantified using a BCA protein assay kit (Beyotime, P0012). A total of 15–20 μg of protein was separated by 10% SDS–PAGE and transferred to PVDF membranes. The membranes were blocked with 5% skim milk or 5% BSA (1 h, room temperature) and then incubated with primary antibodies overnight at 4 °C. After three TBST washes, the membranes were incubated with an HRP-conjugated secondary antibody (1 h, room temperature). The proteins were detected using ECL reagents. The antibodies used are listed in Supplementary Table 3.

ELISA
Activin B concentrations in tumor lysates were measured as follows: Tumors were homogenized in PBS containing protease inhibitors and centrifuged at 5000×*g* for 5 min (4 °C), and the concentrations of Activin B in the supernatants were measured using an ELISA kit (JL20394; Jianglaibio) according to the manufacturer's instructions.

In vivo ABT-263 treatment
To eliminate senescent cells in the diabetic tumor microenvironment, HFD + STZ C57BL/6J mice bearing orthotopic tumors (KPC and Pan02 graft models) received a daily oral administration of ABT-263 (100 mg/kg, HY-10087, Navitoclax, MedChemExpress) or vehicle for 7 consecutive days (7–13 days after injection). The mice were sacrificed on day 14 after injection. Fasting blood glucose was measured after the final dose. Tumors were sampled and embedded in OCT for double immunofluorescence staining. Chow-fed C57BL/6J mice receiving vehicle served as negative controls.

In vivo bimagrumab treatment
To assess the therapeutic effects of INHBB receptor inhibition on diabetic tumors, tumor-bearing chow and HFD + STZ mice (KPC and Pan02 models) received weekly subcutaneous injections of 20 mg/kg bimagrumab (HY-P99355, BYM338, MedChemExpress) or the IgG1λ1 isotype control (HY-P99992; MedChemExpress) on days 7 and 14 after injection. After two doses, the mice were sacrificed on day 16. Diabetic tumor-bearing mice additionally received daily intraperitoneal injections of metformin (250 mg/kg, D150959; Sigma–Aldrich) for 7 days (days 7–13). Fasting blood glucose was measured after the final dose. Bilateral tibialis anterior muscles were harvested to assess posttreatment changes in muscle mass.

Survival analysis
Cox regression was used to assess the association between diabetes history and overall survival in primary pancreatic cancer cohorts (MSK-IMPACT and Xijing Hospital). Significant univariable Cox factors were included in the multivariate analysis. Kaplan–Meier and restricted mean survival time (RMST) analyses were performed to determine the associations between overall survival and diabetes history/preoperative fasting glucose using R packages (survival, version 3.5–7; survRM2, version 1.0.4). The Kaplan–Meier plotter database (https://kmplot.com/analysis) was used to evaluate the prognostic value of INHBB expression for overall survival and disease-free survival in pancreatic cancer patients.

Statistics and reproducibility
Group differences in categorical variables were assessed by Pearson chi-square tests. For continuous variables, nonnormally distributed data were analyzed using Wilcoxon rank-sum tests, whereas normally distributed data were analyzed by Student's *t*-tests. In the RNA-seq analysis, intergroup gene expression differences were evaluated by Wilcoxon test. Gene expression and enrichment score correlations were examined using Spearman correlation analysis. Unpaired two-tailed Student's *t*-tests were used for two-group comparisons. Multigroup comparisons were performed by one-way or two-way ANOVA followed by appropriate post hoc tests. The bars represent the mean ± standard deviation (SD). $P < 0.05$ was considered to indicate statistical significance. Analyses were performed in Prism 8.0 (GraphPad). For representative results shown, experiments were repeated at least three times with similar results. No data were excluded. Mice were randomized to control or experimental groups. Experiments were unblinded unless otherwise specified.

Reporting summary
Further information on research design is available in the Nature Portfolio Reporting Summary linked to this article.

Data availability
Raw sequencing data generated in this study are deposited in the NCBI Sequence Read Archive (SRA) under accession codes PRJNA1182960 (bulk RNA-seq data from the chow and HFD + STZ mice) and PRJNA1182991 (scRNA-seq data from the chow and HFD + STZ mice). scRNA-seq data for PDAC patients were obtained from the Genome Sequence Archive database (GSA, accession: CRA001160). Published bulk RNA-seq datasets analyzed are available in the Gene Expression Omnibus (GEO) under accessions GSE266899, GSE111127, GSE163568, and GSE40403. We have all relevant approvals from China's Ministry of Science and Technology related to the export of genetic information and materials relevant to this work. Source data are provided with this paper.

References
1. Stoop, T. F. et al. Pancreatic cancer. *Lancet* **405**, 1182–1202 (2025).
2. Roy, A. et al. Diabetes and pancreatic cancer: exploring the two-way traffic. *World J. Gastroenterol.* **27**, 4939–4962 (2021).
3. Hank, T. et al. Diabetes mellitus is associated with unfavorable pathologic features, increased postoperative mortality, and worse

long-term survival in resected pancreatic cancer. *Pancreatology* **20**, 125–131 (2020).
4. Chu, C. K. et al. Preoperative diabetes mellitus and long-term survival after resection of pancreatic adenocarcinoma. *Ann. Surg. Oncol.* **17**, 502–513 (2010).
5. Walter, U., Kohlert, T., Rahbari, N. N., Weitz, J. & Welsch, T. Impact of preoperative diabetes on long-term survival after curative resection of pancreatic adenocarcinoma: a systematic review and meta-analysis. *Ann. Surg. Oncol.* **21**, 1082–1089 (2014).
6. Hanahan, D. Hallmarks of cancer: new dimensions. *Cancer Discov.* **12**, 31–46 (2022).
7. Maishi, N. & Hida, K. Tumor endothelial cells accelerate tumor metastasis. *Cancer Sci.* **108**, 1921–1926 (2017).
8. Leone, P. et al. Endothelial cells in tumor microenvironment: insights and perspectives. *Front. Immunol.* **15**, 1367875 (2024).
9. Aird, W. C. Endothelial cell heterogeneity. *Cold Spring Harb. Perspect. Med.* **2**, a006429 (2012).
10. Sobierajska, K., Ciszewski, W. M., Sacewicz-Hofman, I. & Niewiarowska, J. Endothelial cells in the tumor microenvironment. *Adv. Exp. Med. Biol.* **1234**, 71–86 (2020).
11. Zeng, Q. et al. Understanding tumor endothelial cell heterogeneity and function from single-cell omics. *Nat. Rev. Cancer* **23**, 544–564 (2023).
12. Hernandez-Segura, A., Nehme, J. & Demaria, M. Hallmarks of cellular senescence. *Trends Cell Biol.* **28**, 436–453 (2018).
13. Zhu, H. et al. Oncogene-induced senescence: from biology to therapy. *Mech. Ageing Dev.* **187**, 111229 (2020).
14. Rattanavirotkul, N., Kirschner, K. & Chandra, T. Induction and transmission of oncogene-induced senescence. *Cell Mol. Life Sci.* **78**, 843–852 (2021).
15. Marin, I. et al. Cellular senescence is immunogenic and promotes antitumor immunity. *Cancer Discov.* **13**, 410–431 (2023).
16. Chen, H. A. et al. Senescence rewires microenvironment sensing to facilitate antitumor immunity. *Cancer Discov.* **13**, 432–453 (2023).
17. Kang, T. W. et al. Senescence surveillance of pre-malignant hepatocytes limits liver cancer development. *Nature* **479**, 547–551 (2011).
18. Gabai, Y., Assouline, B. & Ben-Porath, I. Senescent stromal cells: roles in the tumor microenvironment. *Trends Cancer*. https://doi.org/10.1016/j.trecan.2022.09.002 (2022).
19. Wang, B., Han, J., Elisseeff, J. H. & Demaria, M. The senescence-associated secretory phenotype and its physiological and pathological implications. *Nat. Rev. Mol. Cell Biol.* https://doi.org/10.1038/s41580-024-00727-x (2024).
20. Igarashi, N. et al. Hepatocyte growth factor derived from senescent cells attenuates cell competition-induced apical elimination of oncogenic cells. *Nat. Commun.* **13**, 4157 (2022).
21. Yamagishi, R. et al. Gasdermin D-mediated release of IL-33 from senescent hepatic stellate cells promotes obesity-associated hepatocellular carcinoma. *Sci. Immunol.* **7**, eabl7209 (2022).
22. Ye, J. et al. Senescent CAFs mediate immunosuppression and drive breast cancer progression. *Cancer Discov.* **14**, 1302–1323 (2024).
23. Belle, J. I. et al. Senescence defines a distinct subset of myofibroblasts that orchestrates immunosuppression in pancreatic cancer. *Cancer Discov.* **14**, 1324–1355 (2024).
24. Haston, S. et al. Clearance of senescent macrophages ameliorates tumorigenesis in KRAS-driven lung cancer. *Cancer Cell* **41**, 1242–1260.e1246 (2023).
25. Prieto, L. I. et al. Senescent alveolar macrophages promote early-stage lung tumorigenesis. *Cancer Cell* **41**, 1261–1275.e1266 (2023).
26. Coppe, J. P. et al. Senescence-associated secretory phenotypes reveal cell-nonautonomous functions of oncogenic RAS and the p53 tumor suppressor. *PLoS Biol.* **6**, 2853–2868 (2008).
27. Ruscetti, M. et al. Senescence-induced vascular remodeling creates therapeutic vulnerabilities in pancreas cancer. *Cell* **181**, 424–441.e421 (2020).
28. Hwang, H. J. et al. Endothelial cells under therapy-induced senescence secrete CXCL11, which increases aggressiveness of breast cancer cells. *Cancer Lett.* **490**, 100–110 (2020).
29. Palmer, A. K., Gustafson, B., Kirkland, J. L. & Smith, U. Cellular senescence: at the nexus between ageing and diabetes. *Diabetologia* **62**, 1835–1841 (2019).
30. Bloom, S. I., Islam, M. T., Lesniewski, L. A. & Donato, A. J. Mechanisms and consequences of endothelial cell senescence. *Nat. Rev. Cardiol.* **20**, 38–51 (2023).
31. Spinelli, R. et al. Increased cell senescence in human metabolic disorders. *J. Clin. Invest*. https://doi.org/10.1172/JCI169922 (2023).
32. Liu, J. et al. Cellular senescence: a bridge between diabetes and microangiopathy. *Biomolecules*. https://doi.org/10.3390/biom14111361 (2024).
33. Narasimhan, A., Flores, R. R., Robbins, P. D. & Niedernhofer, L. J. Role of cellular senescence in type II diabetes. *Endocrinology*. https://doi.org/10.1210/endocr/bqab136 (2021).
34. Goveia, J. et al. An integrated gene expression landscape profiling approach to identify lung tumor endothelial cell heterogeneity and angiogenic candidates. *Cancer Cell* **37**, 421 (2020).
35. Niu, N. et al. Tumor cell-intrinsic epigenetic dysregulation shapes cancer-associated fibroblasts heterogeneity to metabolically support pancreatic cancer. *Cancer Cell* **42**, 869–884.e869 (2024).
36. Peng, J. et al. Single-cell RNA-seq highlights intra-tumoral heterogeneity and malignant progression in pancreatic ductal adenocarcinoma. *Cell Res.* **29**, 725–738 (2019).
37. Pan, X. et al. Tumor vasculature at single-cell resolution. *Nature* **632**, 429–436 (2024).
38. Childs, B. G. et al. Senescent cells: an emerging target for diseases of ageing. *Nat. Rev. Drug Discov.* **16**, 718–735 (2017).
39. Schmitt, C. A., Wang, B. & Demaria, M. Senescence and cancer—role and therapeutic opportunities. *Nat. Rev. Clin. Oncol.* **19**, 619–636 (2022).
40. de Magalhaes, J. P. Cellular senescence in normal physiology. *Science* **384**, 1300–1301 (2024).
41. Kaefer, A. et al. Mechanism-based pharmacokinetic/pharmacodynamic meta-analysis of navitoclax (ABT-263) induced thrombocytopenia. *Cancer Chemother. Pharmacol.* **74**, 593–602 (2014).
42. Duan, J. L. et al. Shear stress-induced cellular senescence blunts liver regeneration through Notch-sirtuin 1-P21/P16 axis. *Hepatology* **75**, 584–599 (2022).
43. Wieland, E. et al. Endothelial Notch1 activity facilitates metastasis. *Cancer Cell***31**, 355–367 (2017).
44. Lim, R. et al. Deubiquitinase USP10 regulates Notch signaling in the endothelium. *Science* **364**, 188–193 (2019).
45. Heymsfield, S. B. et al. Effect of bimagrumab vs placebo on body fat mass among adults with type 2 diabetes and obesity: a phase 2 randomized clinical trial. *JAMA Netw. Open* **4**, e2033457 (2021).
46. Wu, Z., Uhl, B., Gires, O. & Reichel, C. A. A transcriptomic pan-cancer signature for survival prognostication and prediction of immunotherapy response based on endothelial senescence. *J. Biomed. Sci.* **30**, 21 (2023).
47. Gilbert, L. A. & Hemann, M. T. DNA damage-mediated induction of a chemoresistant niche. *Cell* **143**, 355–366 (2010).
48. Bent, E. H., Gilbert, L. A. & Hemann, M. T. A senescence secretory switch mediated by PI3K/AKT/mTOR activation controls chemoprotective endothelial secretory responses. *Genes Dev.* **30**, 1811–1821 (2016).
49. Wang, D. et al. Sunitinib facilitates metastatic breast cancer spreading by inducing endothelial cell senescence. *Breast Cancer Res.* **22**, 103 (2020).

50. Liu, Y. et al. Klotho-mediated targeting of CCL2 suppresses the induction of colorectal cancer progression by stromal cell senescent microenvironments. *Mol. Oncol.* **13**, 2460–2475 (2019).
51. Gorelov, R. et al. Dissecting the impact of differentiation stage, replicative history, and cell type composition on epigenetic clocks. *Stem Cell Rep*. https://doi.org/10.1016/j.stemcr.2024.07.009 (2024).
52. Assouline, B. et al. Senescent cancer-associated fibroblasts in pancreatic adenocarcinoma restrict $CD8^+$ T cell activation and limit responsiveness to immunotherapy in mice. *Nat. Commun.* **15**, 6162 (2024).
53. Salam, R. et al. Cellular senescence in malignant cells promotes tumor progression in mouse and patient glioblastoma. *Nat. Commun.* **14**, 441 (2023).
54. Fournier, F. et al. Obesity triggers tumoral senescence and renders poorly immunogenic malignancies amenable to senolysis. *Proc. Natl. Acad. Sci. USA* **120**, e2209973120 (2023).
55. Ji, J. et al. Radiotherapy-induced astrocyte senescence promotes an immunosuppressive microenvironment in glioblastoma to facilitate tumor regrowth. *Adv. Sci.* **11**, e2304609 (2024).
56. Saleh, T. et al. Clearance of therapy-induced senescent tumor cells by the senolytic ABT-263 via interference with BCL-X_L–BAX interaction. *Mol. Oncol.* **14**, 2504–2519 (2020).
57. Siebel, C. & Lendahl, U. Notch signaling in development, tissue homeostasis, and disease. *Physiol. Rev.* **97**, 1235–1294 (2017).
58. Liu, Y., Zhou, Q., Zou, G. & Zhang, W. Inhibin subunit beta B (INHBB): an emerging role in tumor progression. *J. Physiol. Biochem*. https://doi.org/10.1007/s13105-024-01041-y (2024).
59. Hongu, T. et al. Perivascular tenascin C triggers sequential activation of macrophages and endothelial cells to generate a pro-metastatic vascular niche in the lungs. *Nat. Cancer* **3**, 486–504 (2022).
60. Hofbauer, L. C. et al. Bimagrumab to improve recovery after hip fracture in older adults: a multicentre, double-blind, randomised, parallel-group, placebo-controlled, phase 2a/b trial. *Lancet Healthy Longev.* **2**, e263–e274 (2021).
61. Ma, J. D., Heavey, S. F., Revta, C. & Roeland, E. J. Novel investigational biologics for the treatment of cancer cachexia. *Expert Opin. Biol. Ther.* **14**, 1113–1120 (2014).
62. Hatakeyama, S. et al. ActRII blockade protects mice from cancer cachexia and prolongs survival in the presence of anti-cancer treatments. *Skelet. Muscle* **6**, 26 (2016).
63. Queiroz, A. L. et al. Blocking ActRIIB and restoring appetite reverses cachexia and improves survival in mice with lung cancer. *Nat. Commun.* **13**, 4633 (2022).
64. Padua, D. & Massague, J. Roles of TGFbeta in metastasis. *Cell Res.* **19**, 89–102 (2009).
65. Duan, J. L. et al. Notch-regulated c-Kit-positive liver sinusoidal endothelial cells contribute to liver zonation and regeneration. *Cell Mol. Gastroenterol. Hepatol.* **13**, 1741–1756 (2022).
66. Li, W. V. & Li, J. J. An accurate and robust imputation method scImpute for single-cell RNA-seq data. *Nat. Commun.* **9**, 997 (2018).

Acknowledgements

This work was supported by grants from the National Natural Science Foundation of China (82325007, funding to Lin Wang) and the National Key Research and Development Program of China (2021YFA1100502, funding to Lin Wang).

Author contributions

Y.W.L. and J.L.D. performed in vivo experiments and collected data; Z.J.J. and Z.Y. performed in vitro experiments and collected data; J.J.L. and P.S. performed histological analysis; Z.Q.F. and Z.S.Y. performed single-cell RNA sequencing and bulk RNA sequencing analysis; F.H. provided statistical guidance; K.F.D. and L.W. conceived and supervised the study.

Competing interests

The authors declare no competing interests.

Additional information

Supplementary information The online version contains supplementary material available at https://doi.org/10.1038/s41467-025-63801-8.

Correspondence and requests for materials should be addressed to Ke-Feng Dou or Lin Wang.

Peer review information *Nature Communications* thanks the anonymous reviewers for their contribution to the peer review of this work. A peer review file is available.